Electronic Supporting Information

Using nickel manganese oxide catalysts for efficient water oxidation

Prashanth W. Menezes,[a] Arindam Indra,[a] Ophir Levy,[a] Kamalakannan Kailasam,[a] Vitaly Gutkin,[b] Johannes Pfrommer,[a] and Matthias Driess*[a]

[a]*Metalorganic Chemistry and Inorganic Materials, Department of Chemistry, Technische Universität Berlin, Strasse des 17 Juni 135, Sekr. C2, D-10623 Berlin, Germany*

[b]*The Harvey M. Krueger Family Center for Nanoscience and Nanotechnology, The Hebrew University of Jerusalem, Edmond J. Safra Campus, Givat Ram, Jerusalem, 91904, Israel*

Chemicals

All chemical reagents (analytical grade) were used as received without any further purification. Commercially available nickel(II) acetate tetrahydrate ($Ni(CH_3COO)_2\cdot4H_2O$), manganese(II) acetate tetrahydrate ($Mn(CH_3COO)_2\cdot4H_2O$), manganese oxides (MnO_2, Mn_2O_3, Mn_3O_4), ceric ammonium nitrate ($(NH_4)_2[Ce(NO_3)_6]$), sodium peroxodisulfate ($Na_2S_2O_8$) and tris(bipyridine)ruthenium(II) chloride hexahydrate ($[Ru(bpy)_3]Cl_2\cdot6H_2O$) were obtained from Alfa Aesar whereas, cetyltrimethylammonium bromide (CTAB), ammonium oxalate dihydrate ($(NH_4)_2C_2O_4\cdot2H_2O$ was purchased from Alfa Aesar. Deionised water was used throughout the experiment.

Instrumental

PXRD was carried out to determine the phase identification of the samples using a Bruker AXS D8 advanced automatic diffractometer equipped with a position sensitive detector (PSD) and a curved germanium (111) primary monochromator. The radiation used was Cu-*Kα* (λ = 1.5418 Å). The XRD patterns were recorded in the range of $5° < 2\theta < 80°$ and subsequently the diffraction pattern fitting were performed using the program WinxPow. Similarly, the structural models were drawn with the program DIAMOND version 3.0.

The chemical composition of the precursor was confirmed by ICP-AES on a Thermo Jarrell Ash Trace Scan analyser. First of all, the samples were dissolved in acid solutions (aqua regia) and then the results of three independent measurements were averaged which were in accordance with the chemical formulae. The quantification of the precursor and oxide was also estimated by the elemental analyses which were performed on a Flash EA 112 Thermo Finnigan elemental analyser.

To evaluate size and morphology SEM was used and EDX analyses were used to semi-quantitatively determine the nickel and manganese present on the sample surfaces. The samples were placed on a silicon wafer and the measurements were carried on a LEO DSM 982 microscope integrated with EDX (EDAX, Appollo XPP). Data handling and analysis were conducted with the software package EDAX.

The microstructure of the presented materials was investigated by TEM analysis. A small amount of the sample powder was placed on a TEM-grid (carbon film on 300 mesh Cu-grid, Plano GmbH, Wetzlar, Germany). The microstructure (morphology, particle size, phase composition, crystallinity) of the samples was studied by a FEI Tecnai G^2 20 S-TWIN transmission electron microscope (FEI Company, Eindhoven, Netherlands) equipped with a LaB_6-source at 200 kV acceleration voltage. EDX analysis were carried out with an EDAX r-TEM SUTW Detector (Si (Li)-detector). Images were recorded with a GATAN MS794 P CCD-camera. Both SEM and TEM experiments were carried out at the Zentrum für Elektronenmikroskopie (ZELMI) of the TU Berlin.

The surface area and the pore size distributions were carried out on a Quantachrome Autosorb-1 apparatus. Nitrogen adsorption/desorption isotherms were determined at -196 ˚C after degassing the sample at 180 ˚C overnight. The BET surface areas (S_{BET}) were estimated by adsorption data in a relative pressure range from 0.05 to 0.5

Simultaneous constant rate TGA analysis of all oxalate precursors was performed on a Rubotherm set up. The samples dried at 80 ˚C overnight and were placed in an open alumina crucible and heated at 5 ˚C/min to 600 ˚C in a continuous nitrogen gas flow and cooled down to the room temperature. The TG curves were corrected by subtraction of a blank run and the solid product obtained after TGA analysis was further examined by PXRD.

The presence of different modes of vibrations of the precursor and the metal oxides were investigated using a BIORAD FTS 6000 FTIR spectrometer under attenuated total reflection (ATR) conditions. The data were recorded in the range of 400–4000 cm^{-1} with the average of thirty two scans at 4 cm^{-1} resolution.

The XPS measurements were performed using a Kratos Axis Ultra X-ray photoelectron spectrometer (Karatos Analytical Ltd., Manchester, UK) using an Al $K\alpha$ monochromatic radiation source (1486.7 eV) with 90° takeoff angle (normal to analyser). The vacuum pressure in the analyzing chamber was maintained at 2×10^{-9} Torr. The high-resolution XPS spectra were collected for C1*s*, O1*s*, Ni2*p* and Mn2*p* levels with pass energy 20 eV and step 0.1 eV. The binding energies were calibrated relative to C1*s* peak energy position as 285.0 eV. Data analyses were performed using Casa XPS (Casa Software Ltd.) and Vision data processing program (Kratos Analytical Ltd.).

The evolved oxygen gas in photochemical water oxidation experiments were quantified by a gas chromatograph (GC). An Agilent 7890A gas chromatograph was used to determine the oxygen content in a headspace. The GC was equipped with a carboxen-1000 column and a thermal conductivity detector (TCD). The carrier gas was argon with a flow rate of 30 mL/min.

Experimental

Synthesis of nickel manganese and nickel oxalate precursors.[1] For $Ni_{0.85}Mn_{0.15}C_2O_4{\cdot}2H_2O$, three micro-emulsions containing cetyltrimethylammonium bromide (CTAB, 2.0 g) as a surfactant, 1-hexanol (20 mL) as co-surfactant and hexane (35 ml) as the lipophilic phase were prepared with an aqueous solution of 0.1 M nickel acetate, 0.1 M manganese acetate and 0.1 M ammonium oxalate. All three micro-emulsions were mixed slowly and stirred overnight at room temperature. The green precipitate then obtained was centrifuged and washed with 1:1 mixture of chloroform and methanol (200 mL) and subsequently dried at 60 ˚C for 12 hours. Similarly, with a ratio of 0.1 M nickel acetate, 0.05 M manganese acetate and 0.1 M ammonium oxalate, $Mn_{0.34}Ni_{0.66}C_2O_4{\cdot}2H_2O$ was produced. By reversing the ratios to 0.1 M manganese acetate and 0.05 M nickel acetate, $Ni_{0.34}Mn_{0.66}C_2O_4{\cdot}2H_2O$ was obtained. Finally, for $NiC_2O_4{\cdot}2H_2O$, only 0.1 M nickel acetate and 0.1 M ammonium oxalate was used.

Synthesis of nickel manganese and nickel oxides.[1] All oxalate precursor were heated to 400 ˚C with the rate of 2 ˚C/min in dry synthetic air (20% O_2, 80% N_2) and kept at 400 ˚C for 8 hours in a tubular furnace and then cooled down naturally to ambient temperature to form Ni_6MnO_8, $MnNi_2O_4$, $NiMn_2O_4$ and NiO oxide phases from the precursors $Ni_{0.85}Mn_{0.15}C_2O_4{\cdot}2H_2O$, $Mn_{0.34}Ni_{0.66}C_2O_4{\cdot}2H_2O$, $Ni_{0.34}Mn_{0.66}C_2O_4{\cdot}2H_2O$ and $NiC_2O_4{\cdot}2H_2O$, respectively.

Oxidant-driven oxygen evolution from water. Chemical oxygen evolution experiments were carried out using aqueous solutions containing ceric ammonium nitrate (CAN) as the sacrificial one electron acceptor. The chemical potential of Ce^{4+} ($E^0 = 1.7$ V *vs* NHE) is indeed sufficient to oxidise water to oxygen in acidic conditions (at pH ~ 1). Therefore, this reaction has been used as the standard test reaction to check the water oxidising property of various transition metal containing oxide catalysts. The oxygen evolution was measured using a Clark-type oxygen electrode system (Strathkelvin, 1302 oxygen electrode and 782 oxygen meters). Prior to the experiments, the electrode was calibrated in air saturated water and in zero oxygen solution (sodium sulphite in water). In a typical reaction, 1 mg catalyst was placed in the reactor which was then degassed by purging nitrogen continuously for the period of 30 minutes. Anaerobic solution (2 mL) of 0.5 M CAN was then injected to the reactor to initiate the chemical water oxidation and oxygen evolution was simultaneously monitored with a Clark electrode under stirring. In each case, the maximum rate of oxygen evolution was calculated using the amount of oxygen production after the first 60 seconds of reaction. After the chemical water oxidation measurements, no change in pH of CAN solution was observed ruling out the possibility of hydrolysis and polymerization of CAN.

Photo-catalytic oxygen evolution from water. Photochemical water oxidation experiments were conducted in a 10 mL quartz reactor fitted with a water jacket by maintaining the temperature at 20 ± 0.5 ^{o}C. $Na_2S_2O_8$ was chosen as two electron sacrificial acceptor whereas $Ru(bpy)_3]^{2+}$ as a photosensitiser. Phosphate buffer in neutral conditions (pH 7) was used not only due to its stability but also because of its higher rates of oxygen formation. A typical run was carried out using 1.5 mg $[Ru(bpy)_3]Cl_2$. $6H_2O$, 3.5 mg $Na_2S_2O_8$ and 1 mL phosphate buffer along with 0.5 mg of catalyst. The reactants were purged with nitrogen for almost an hour to remove all dissolved oxygen from the aqueous solution. The quartz reactor was then illuminated with a continuous output Xenon lamp with the power of 300 W. Visible light was achieved by placing a cutoff filter of 395 nm between the quartz reactor and the light source. Dissolved oxygen concentration during the reaction was measured by a Clark electrode and the rate of oxygen evolution was calculated similar to that of chemical water oxidation (using the amount of oxygen production after the first 60 seconds of reaction). All photochemical reactions were performed at least thrice to ensure good reproducibility and reliability. Oxygen evolution was only seen when all constituents, the light source, the sacrificial electron acceptor, the photosensitiser, and the catalysts were involved in the reaction.[1,2] Interestingly, the catalytic activities were levelled after three minutes of photochemical reaction which is because of the use of lower concentrations and the consumption of the sacrificial electron acceptor and decomposition of $[Ru(bpy)_3]^{2+}$ under visible light. Replacing the solution with sacrificial acceptor and readjusting the pH again resulted in continued water oxidation in the same rate, and has been well described for previously studied transition metal based materials.[1-5]

Oxygen detection by GC. A separate set of controlled experiments were conducted in similar conditions as that of photochemical water oxidation to quantify the oxygen gas in photochemical water oxidation by placing 30 mg catalyst, 25 mg $[Ru(bpy)_3]Cl_2{\cdot}6H_2O$, 100 mg $Na_2S_2O_8$ and 6 mL phosphate buffer solution in a quartz reactor with a headspace of 15 mL. The reactor was then illuminated for two hours using the xenon lamp (300 W, cutoff filter 395 nm) and the O_2 generated in the head space were injected twice and quantitatively analysed by a gas chromatograph (GC).

Electro-catalytic oxygen evolution reaction (OER). Catalytic activity of the nickel manganese and nickel oxide was tested in freshly prepared 0.1 M KOH (pH 13.0) solution using single-compartment three-electrode electrochemical cell. The working electrode was prepared by taking 5 mg of the oxide powder in 2ml of isopropanol and then slowly drop coated on the fluorinated tin oxide (FTO) surface. A few drops of 5 wt% of Nafion were also drop coated on the surface to ensure the enhancement of mechanical stability of the electrodes. A high surface Pt mesh was used as a counter electrode and $Hg/HgSO_4$ (saturated) as a reference electrode. The electrochemical experiments were performed at room temperature using a potentiostat (SP-200, BioLogic Science Instruments) controlled by EC-Lab v10.20 software package. Test runs were carried out with an electrolyte resistance (incl. the electrode) of about 40 Ω; *iR* compensation at 80% was applied. The solution kept unstirred during the experiments. The potentials reported in this work were referenced to the reversible hydrogen electrode (RHE) through RHE calibration, and in 0.1 M KOH at pH 13, $E(RHE) = E(Hg/Hg_2SO_4) + 0.76$ V.

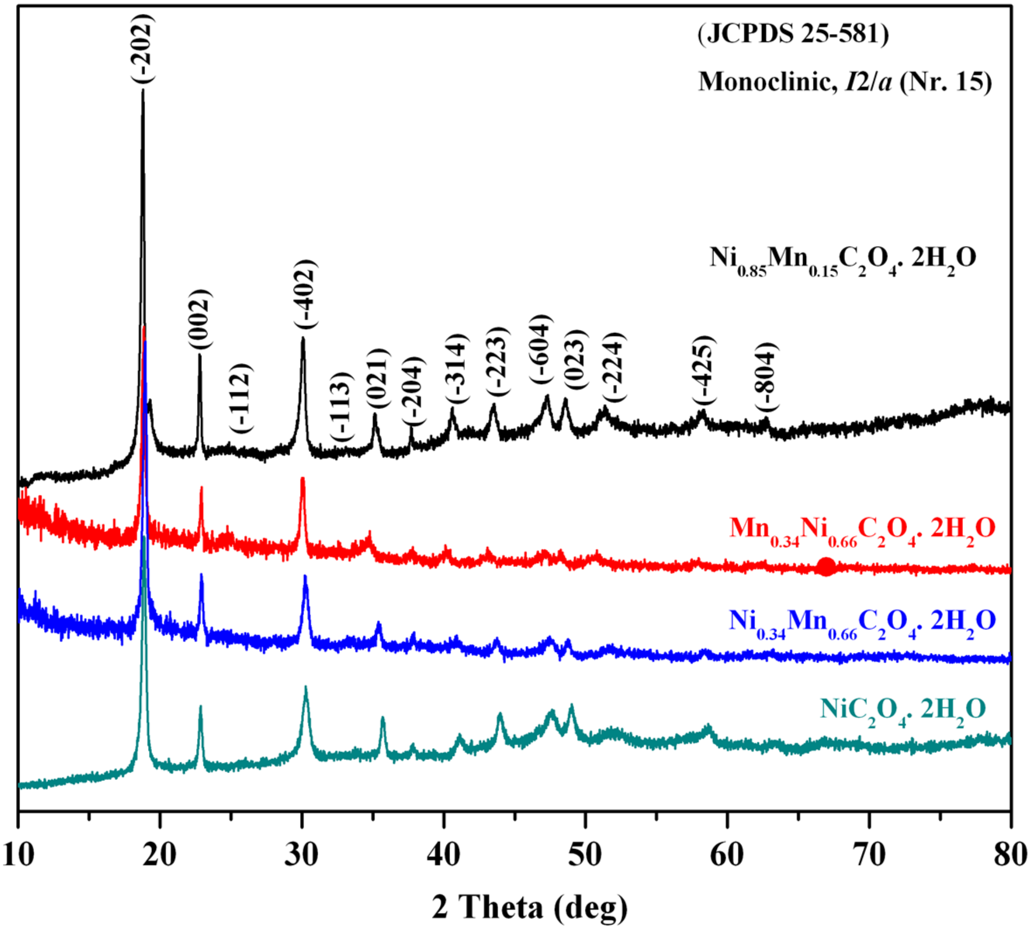

Figure S1. PXRD (in deg) and Miller indices (hkl) of as-prepared mixed nickel manganese and nickel oxalate precursor $Ni_{0.85}Mn_{0.15}C_2O_4{\cdot}2H_2O$, $Mn_{0.34}Ni_{0.66}C_2O_4{\cdot}2H_2O$, $Ni_{0.34}Mn_{0.66}C_2O_4{\cdot}2H_2O$ and $NiC_2O_4{\cdot}2H_2O$ (JCPDS 25-581) *via* inverse micelle approach. The composition of Ni:Mn was derived from EDX and ICP-AES measurements.[6-9]

Table S1. Determination of nickel and manganese ratio in nickel manganese oxides were obtained by ICP-AES and EDX analysis. Three independent measurements were performed for the reliability of the experiments and the average data is presented.

	Ni:Mn (Theoretical)	Ni:Mn (EDX)	Ni:Mn (ICP-AES)
$Ni_{0.85}Mn_{0.15}C_2O_4{\cdot}2H_2O$	6:1	~ 5.9:1	6.01:1
$Mn_{0.34}Ni_{0.66}C_2O_4{\cdot}2H_2O$	2:1	~2:1	1.97:1
$Ni_{0.34}Mn_{0.66}C_2O_4{\cdot}2H_2O$	1:2	~1:2	1.98:1

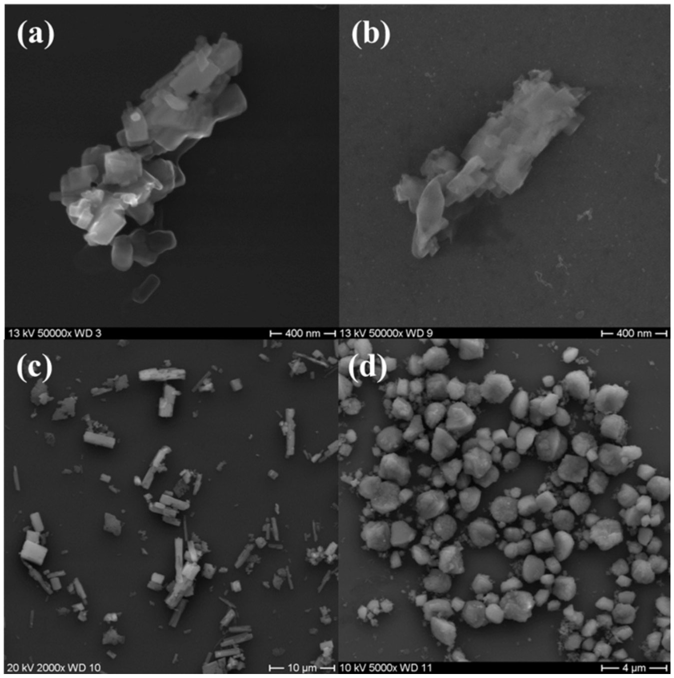

Figure S2. SEM micrographs of (a) $Ni_{0.85}Mn_{0.15}C_2O_4{\cdot}2H_2O$, (b) $Mn_{0.34}Ni_{0.66}C_2O_4{\cdot}2H_2O$, (c) $Ni_{0.34}Mn_{0.66}C_2O_4{\cdot}2H_2O$ and (d) $NiC_2O_4{\cdot}2H_2O$, respectively.

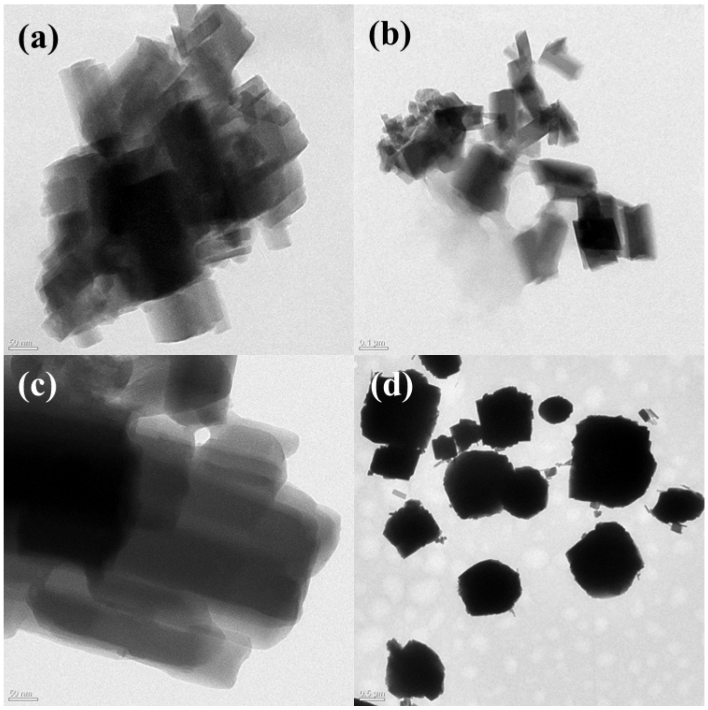

Figure S3. TEM images of (a) $Ni_{0.85}Mn_{0.15}C_2O_4{\cdot}2H_2O$, (b) $Mn_{0.34}Ni_{0.66}C_2O_4{\cdot}2H_2O$, (c) $Ni_{0.34}Mn_{0.66}C_2O_4{\cdot}2H_2O$ and (d) $NiC_2O_4{\cdot}2H_2O$, respectively.

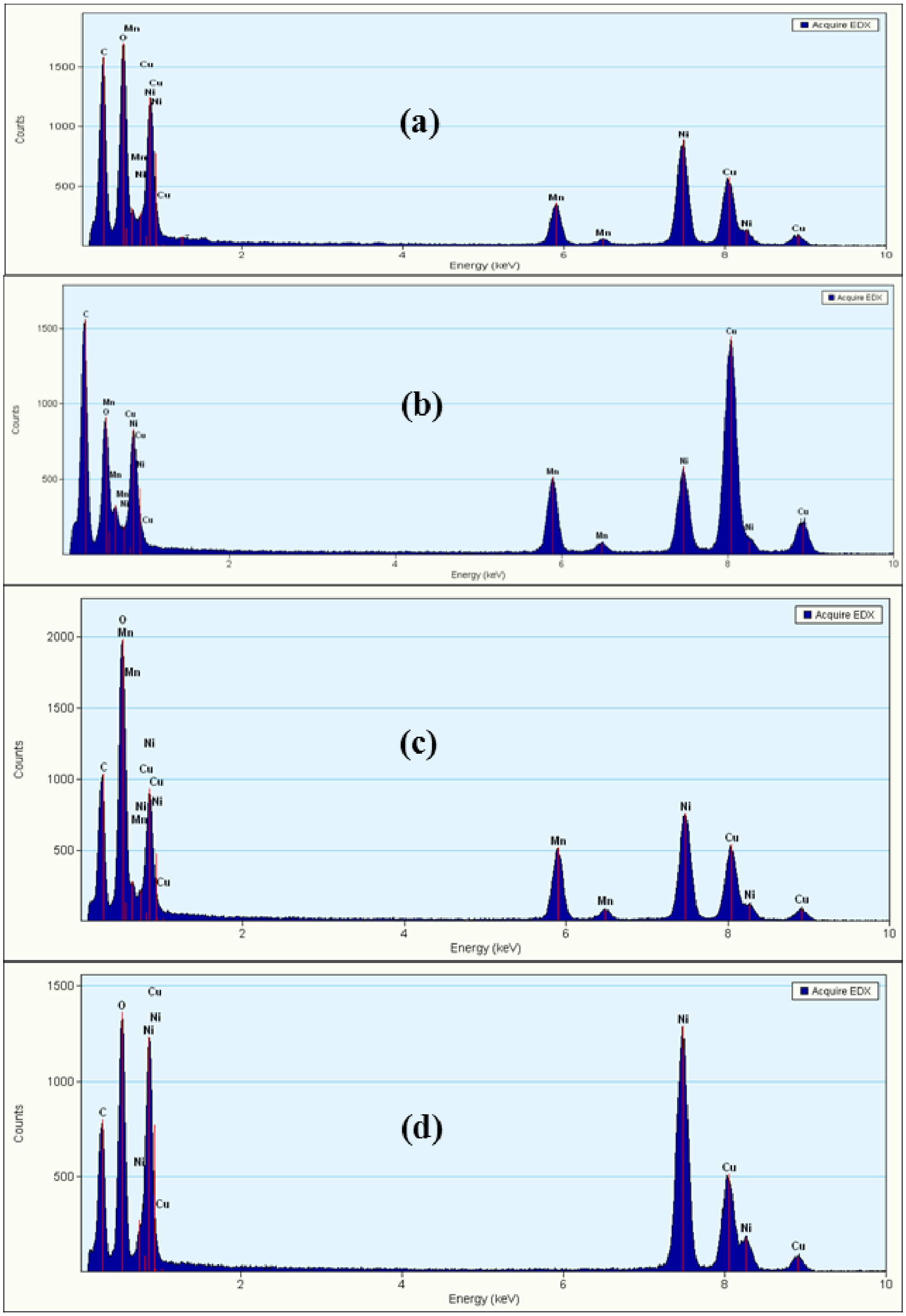

Figure S4. The presence of nickel and/or manganese in a) $Ni_{0.85}Mn_{0.15}C_2O_4{\cdot}2H_2O$, (b) $Mn_{0.34}Ni_{0.66}C_2O_4{\cdot}2H_2O$, (c) $Ni_{0.34}Mn_{0.66}C_2O_4{\cdot}2H_2O$ and (d) $NiC_2O_4{\cdot}2H_2O$ precursors was determined by the EDX measurements. Appearances of peaks for copper are due to TEM grid (carbon film on 300 mesh Cu-grid).

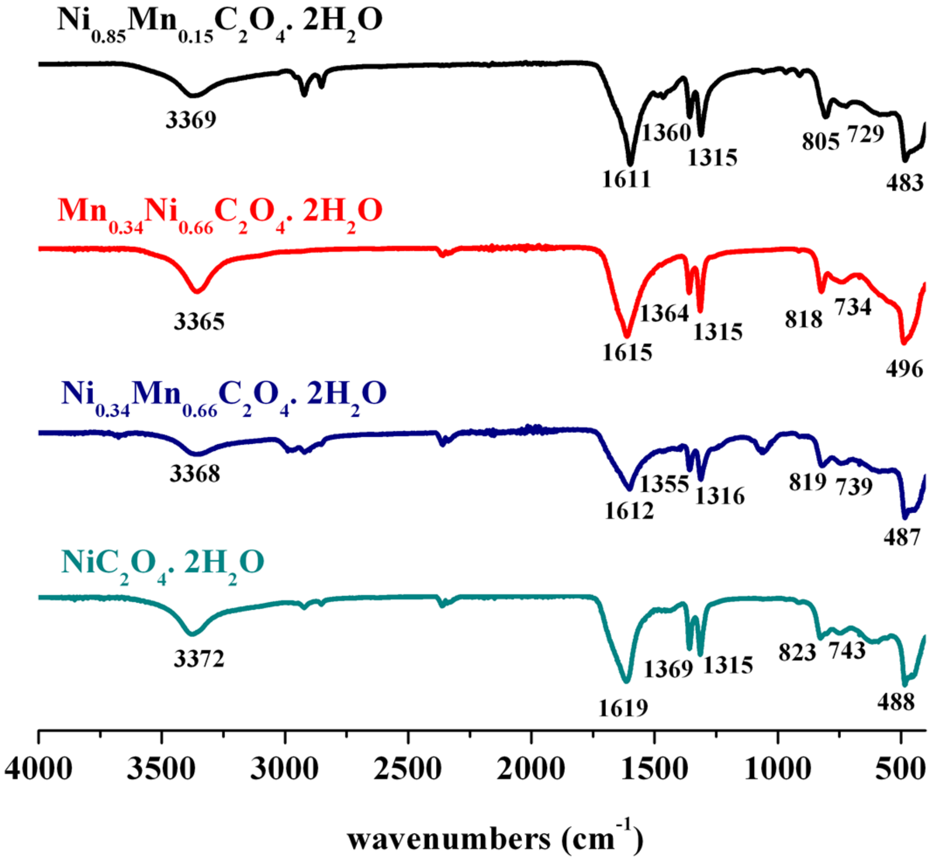

Figure S5. FT-IR transmission spectrum of as prepared nickel manganese oxalate and nickel oxalate precursor.[8, 10, 11]

Table S2. IR absorption maxima (cm^{-1}) of oxalate precursors corresponding to Figure S5 that match well with the maxima previously reported for the metal oxalate precursor.[8,10,11]

$Ni_{0.85}Mn_{0.15}$	$Mn_{0.34}Ni_{0.66}$	$Ni_{0.346}Mn_{0.66}$	Ni	Assignments
3369	3365	3368	3372	γ(OH)(H_2O)
1611	1615	1612	1619	γ_{as}(C–O)
1360	1364	1355	1369	γ_s(C–O)
1315	1315	1316	1315	δ(OCO)
805	818	819	823	γ_s(C–C) + δ(OCO)
729	734	739	743	ρ(H_2O)
483	496	487	488	δ ring

as: asymmetric, s:symmetric, γ:stretching, δ: bending, ρ:scissoring

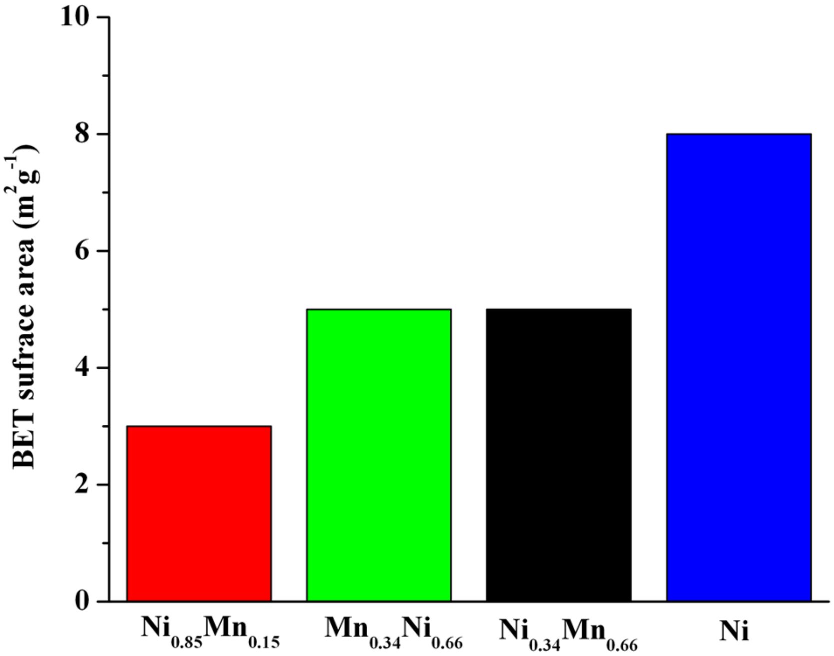

Figure S6. BET surface areas of as prepared $Ni_{0.85}Mn_{0.15}C_2O_4{\cdot}2H_2O$, $Mn_{0.34}Ni_{0.66}C_2O_4{\cdot}2H_2O$, $Ni_{0.34}Mn_{0.66}C_2O_4{\cdot}2H_2O$ and $NiC_2O_4{\cdot}2H_2O$ precursors.

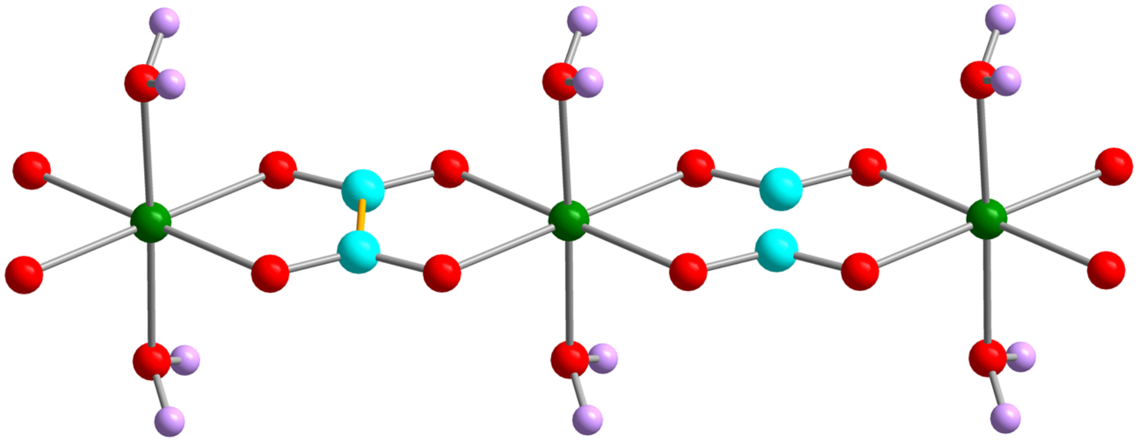

Figure S7. Crystal structure of nickel manganese and nickel oxalate dihydrate precursors which consists of one dimensional chains with each nickel (or mixed nickel manganese) atom coordinated by two bidentate oxalate ligands and two water molecules. Atom colour codes: Ni;green, O;red, C;cyan and H;light pink.[6]

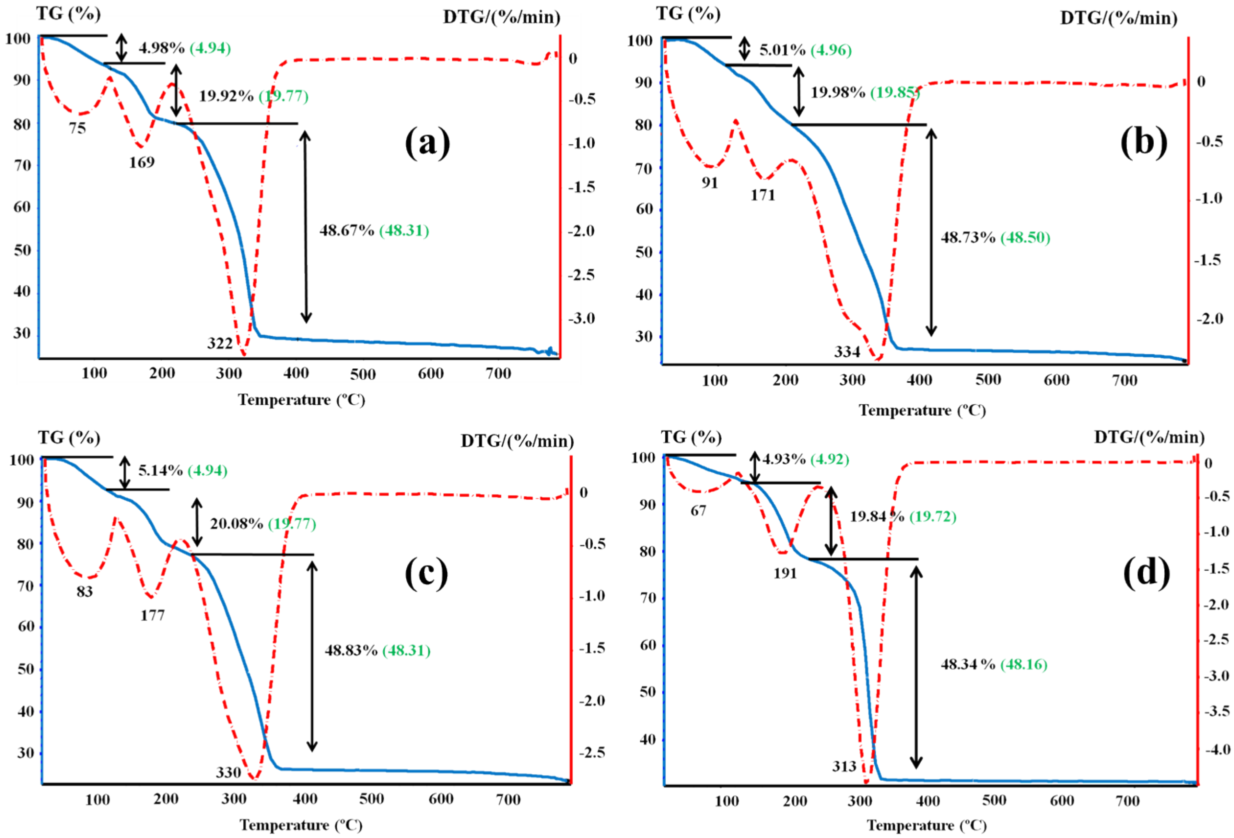

Figure S8. TGA (blue solid line) and its differential (DTG, red dotted line) plot of (a) $Ni_{0.85}Mn_{0.15}C_2O_4{\cdot}2H_2O$, (b) $Mn_{0.34}Ni_{0.66}C_2O_4{\cdot}2H_2O$, (c) $Ni_{0.34}Mn_{0.66}C_2O_4{\cdot}2H_2O$ and (d) $NiC_2O_4{\cdot}2H_2O$ precursors thermally treated from room temperature to 800 ˚C in nitrogen atmosphere at the rate of 5 ˚C/min. In all cases, three distinct mass loss steps were observed. The first mass loss occurs between ~60 to ~120 ˚C, which corresponds to half molecule of absorbed water on the surface with distinct DTG peaks at 75, 91, 83 and 67 ˚C for a–d, respectively. The second mass loss corresponds to the release of two structural water, thus by converting hydrous phases into anhydrous oxalate precursors. This mass loss displays a broad DTG peak at 169, 171, 177 and 191 ˚C for a–d, repsectively. This experimental mass loss (~20%) obtained is consistent with the calculated weight of two water molecules. The third mass loss occurred between 200 to 700 ˚C with a distinct DTG peak at 322, 334, 330 and 313 ˚C for a–d, respectively, transforming the anhydrous oxalate phases into oxide and metallic phases. The mass loss within this step was ~48.6 % and is very close to the calculated values for two molecules of carbon dioxide.[12-14] The PXRD pattern of all phases after the TGA experiments are shown in Figure S9.

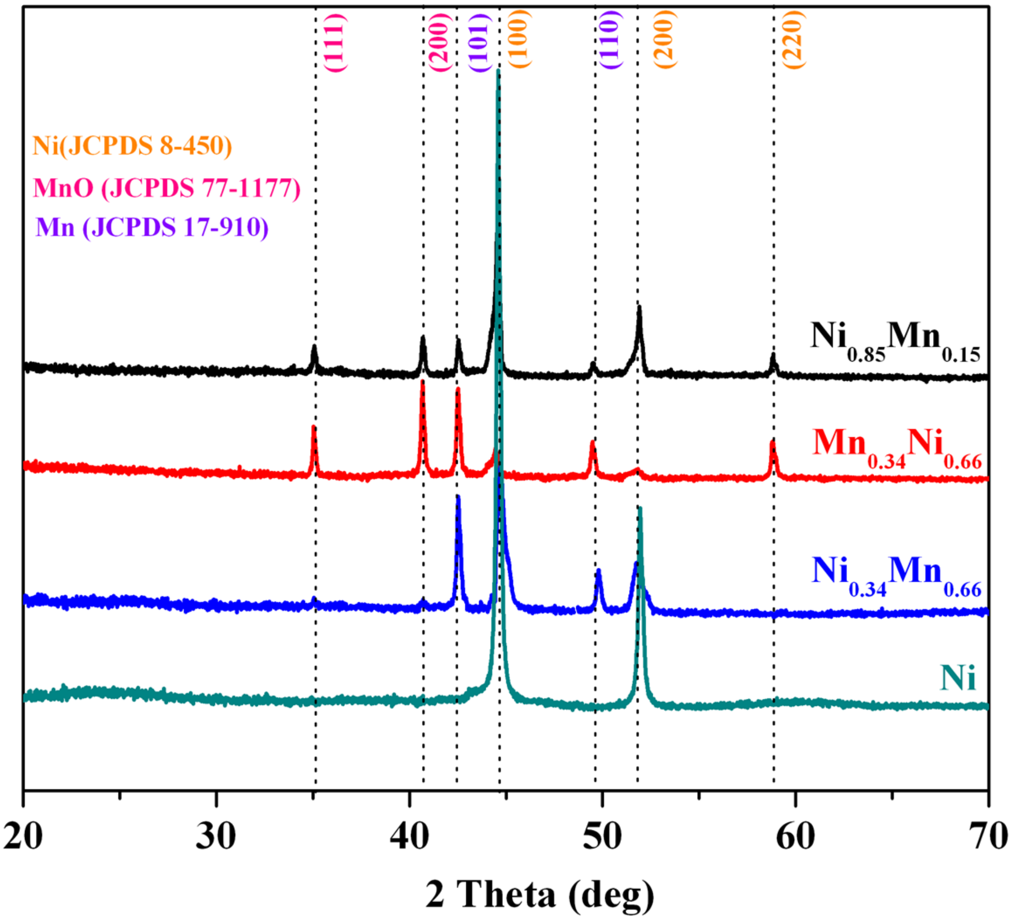

Figure S9. PXRD pattern and Miller indices (hkl) of the decomposition product of nickel manganese and nickel oxalate precursor subjected to thermogravimetric analysis (TGA). The phase was identified as metallic Ni (yellow, JCPDS 8-450), MnO (pink, JCPDS 77-1177) and Mn (violet, JCPDS 17-910).

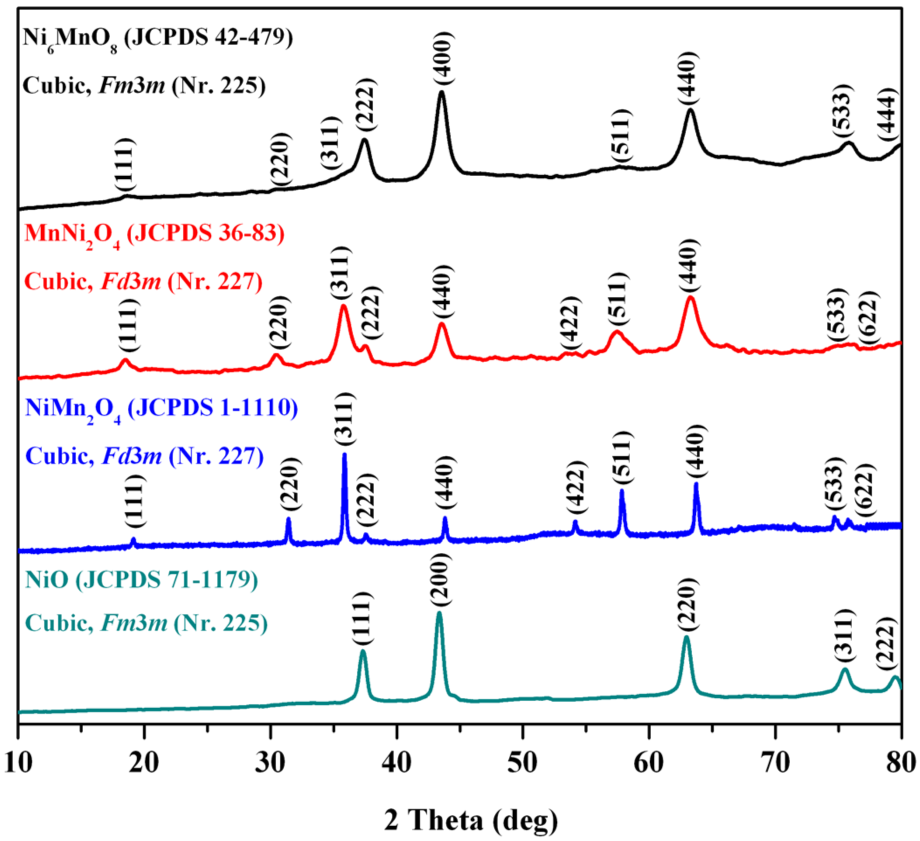

Figure S10. PXRD (in deg) and Miller indices (hkl) of the mixed nickel manganese and nickel oxidese precursor Ni_6MnO_8, $MnNi_2O_4$, $NiMn_2O_4$ and NiO synthesised by heating the respective oxalate precursors. The composition of Ni:Mn was also additionally derived from EDX and ICP-AES measurements.[15-18]

Table S3. Determination of nickel and manganese ratio in nickel manganese oxides were obtained by ICP-AES and EDX. Three independent measurements were performed for the reliability of the experiments and the average data is presented.

	Ni:Mn ratio (Theo.)	Ni:Mn ratio (EDX)	Ni:Mn ratio (ICP-AES)
Ni_6MnO_8	6:1	~6:1	5.98:1
$MnNi_2O_4$	2:1	~2:1	2.01:1
$NiMn_2O_4$	1:2	~1:2	0.99:2

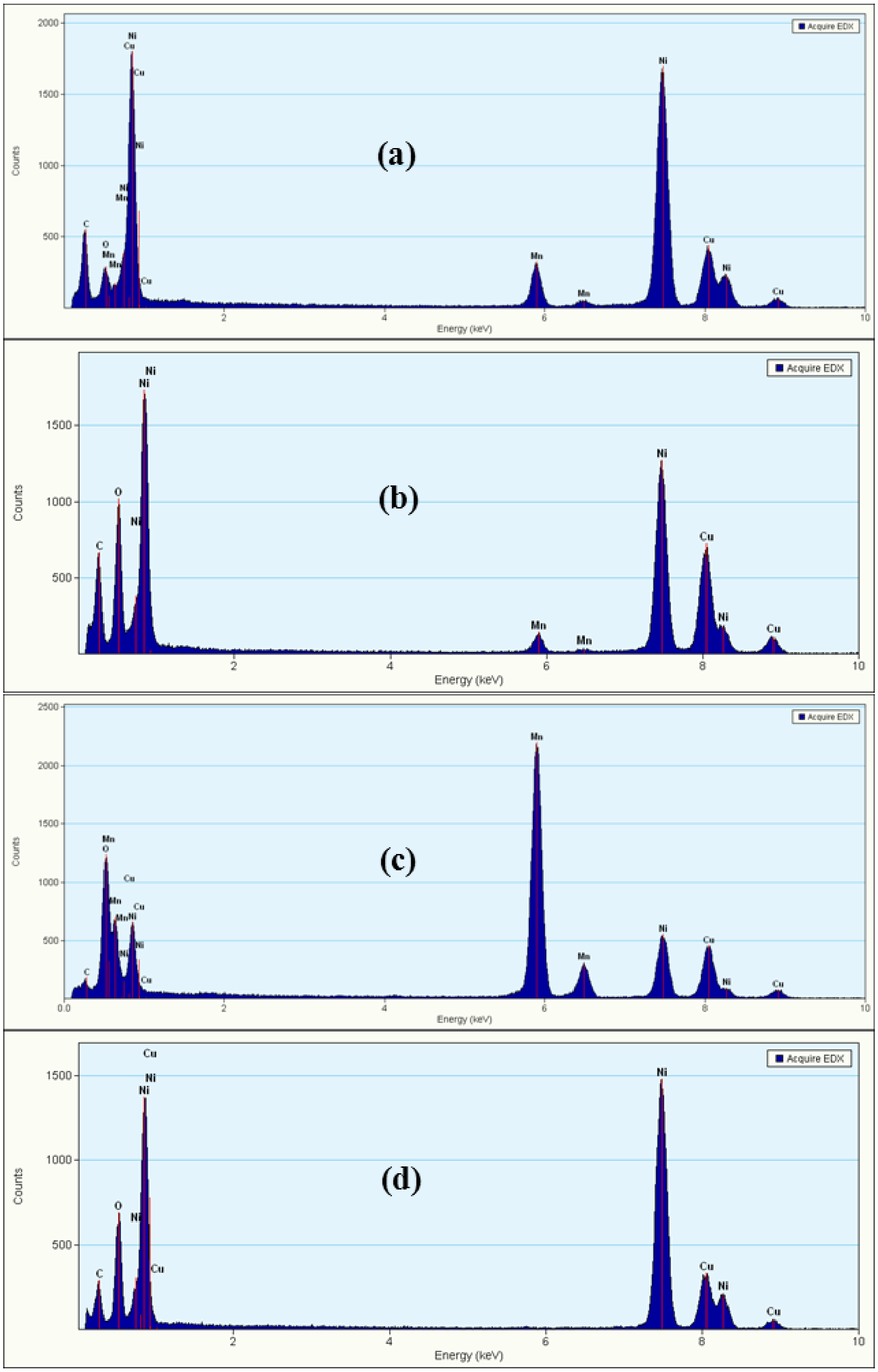

Figure S11. The presence of nickel and/or manganese in (a) Ni_6MnO_8, (b) $MnNi_2O_4$, (c) $NiMn_2O_4$ and (d) NiO was determined by the EDX measurements. Appearances of peaks for copper are due to TEM grid (carbon film on 300 mesh Cu-grid).

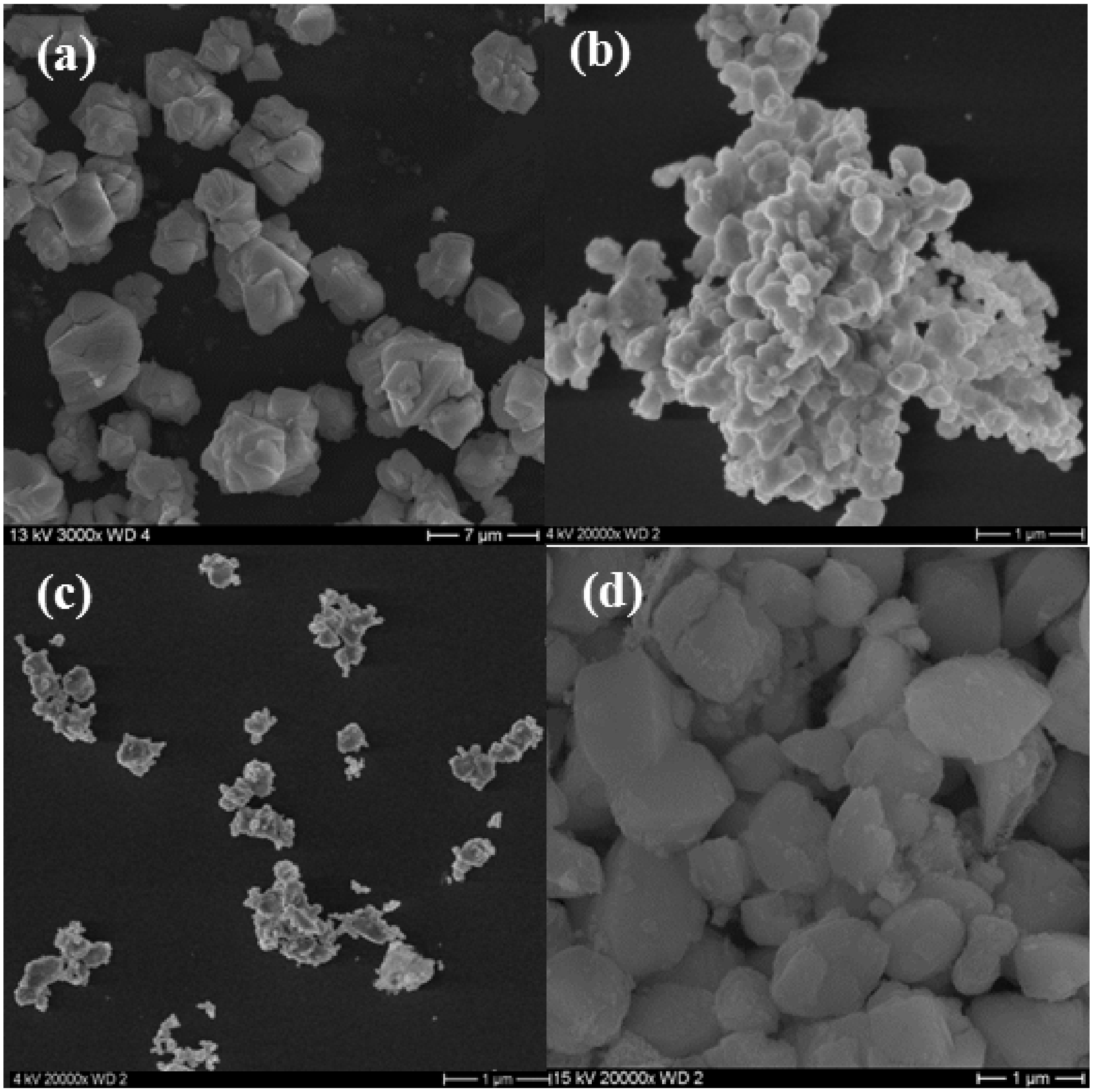

Figure S12. SEM micrographs of (a) Ni_6MnO_8, (b) $MnNi_2O_4$, (c) $NiMn_2O_4$ and (d) NiO, respectively.

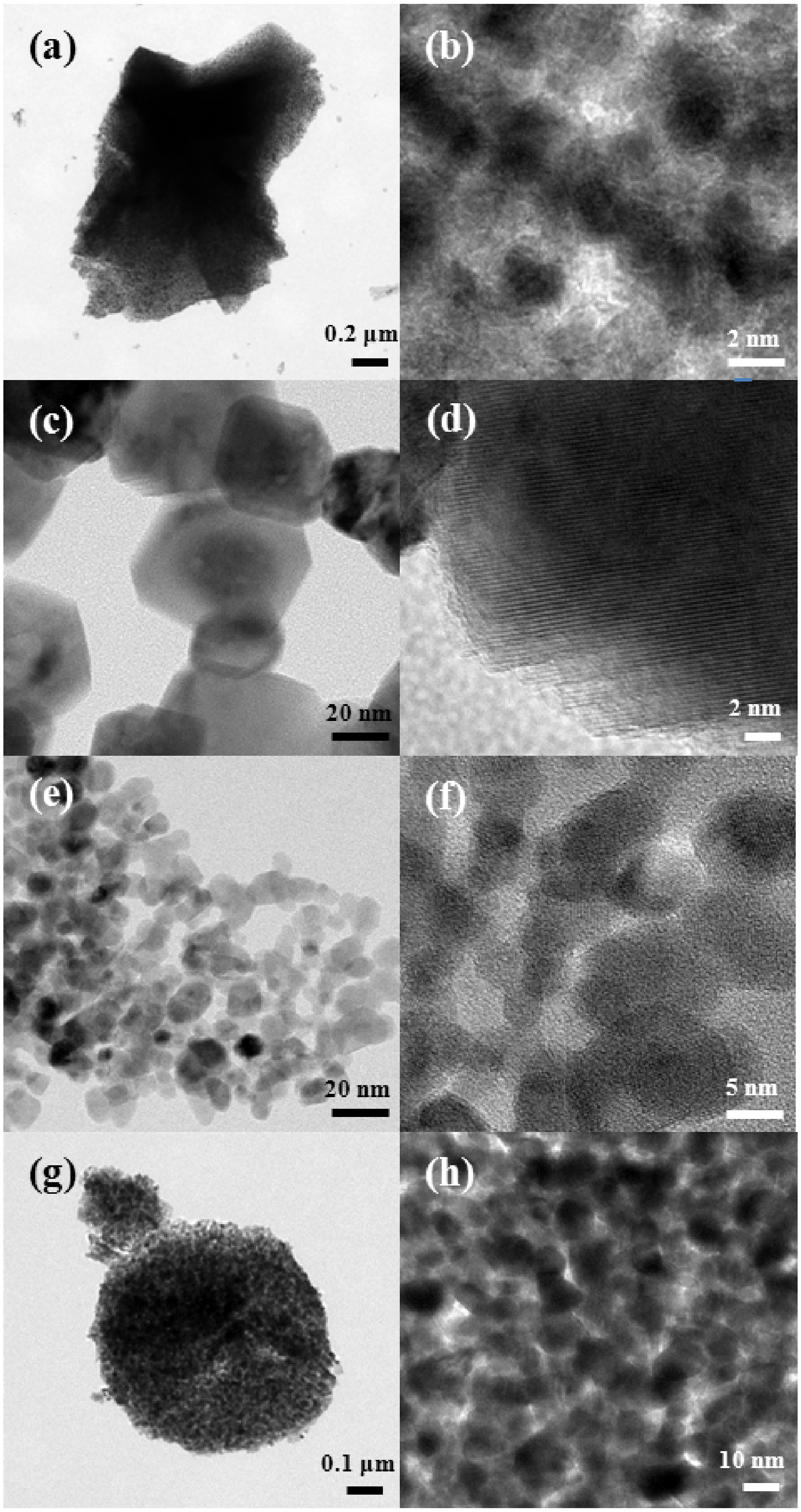

Figure S13. TEM and high resolution TEM images of (a, b) Ni_6MnO_8, (c, d) $MnNi_2O_4$, (e, f) $NiMn_2O_4$ and (g, h) NiO, respectively.

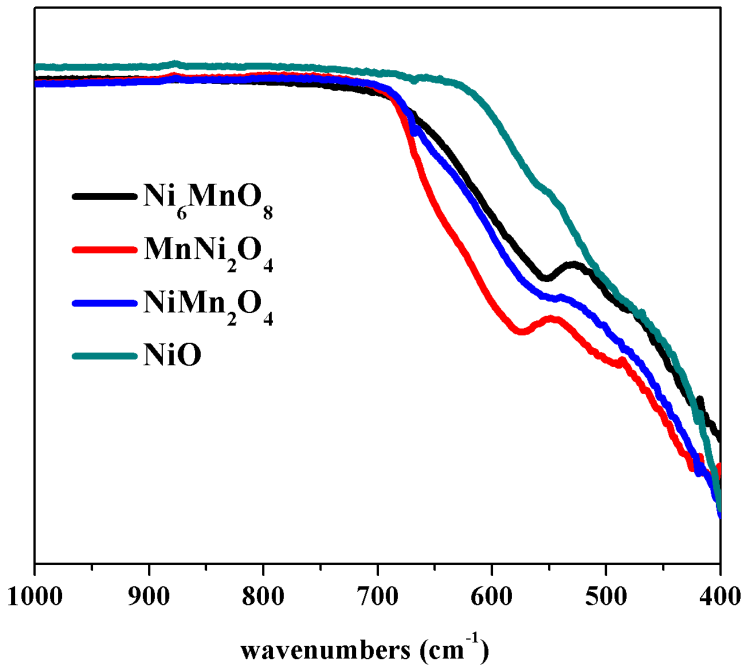

Figure S14. FT-IR transmission spectrum of nickel manganese and nickel oxide in the region 400-1000 cm^{-1} showing symmetric M—O stretching vibrations (betweeb 400-650 cm^{-1}). The shown spectrum is in accordance with the previously reported spectra of manganese and nickel oxides.[13]

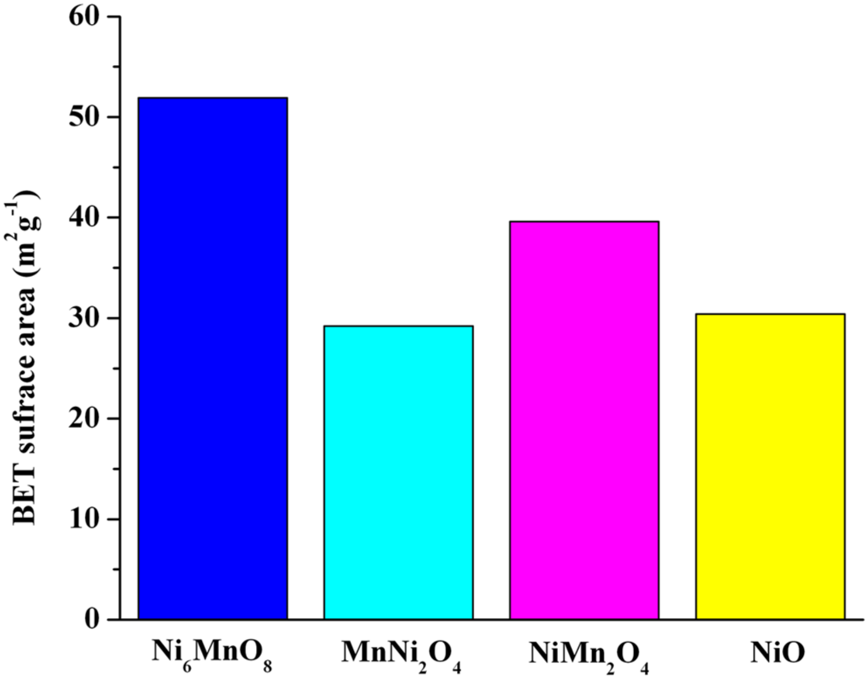

Figure S15. BET surface areas of Ni_6MnO_8, $MnNi_2O_4$, $NiMn_2O_4$ and NiO.

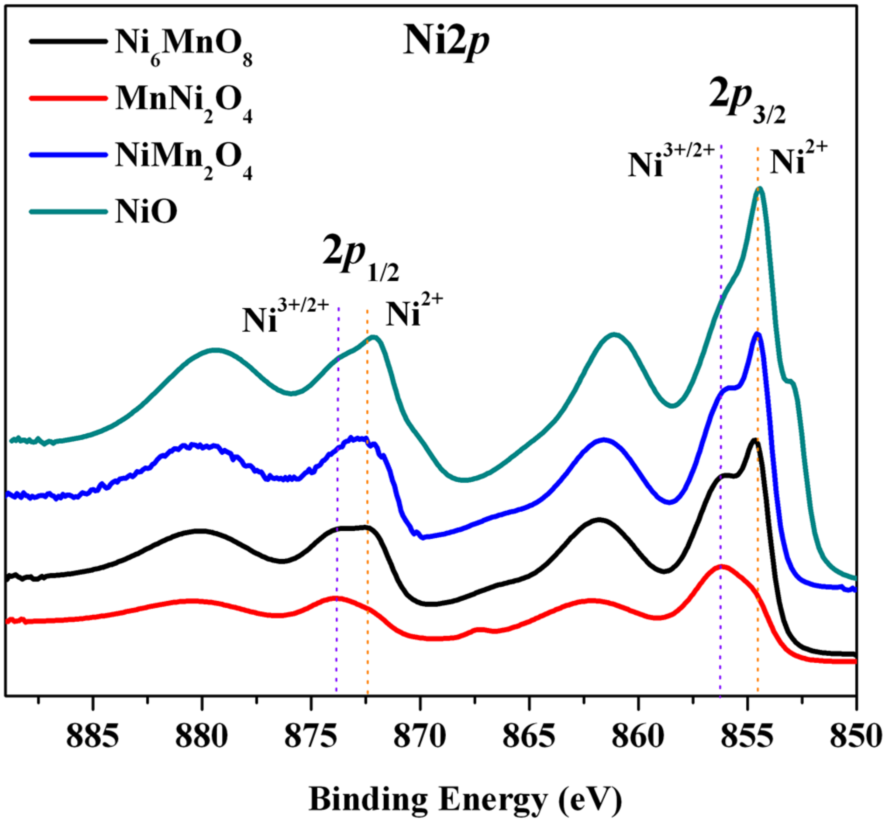

Figure S16. The XPS spectra of the regions containing the Ni2*p* of Ni_6MnO_8, $MnNi_2O_4$, $NiMn_2O_4$ and NiO. The XPS core level spectra of Ni2$p_{3/2}$ for Ni_6MnO_8, $NiMn_2O_4$ and NiO exhibited peaks at ~854.5 eV that could be attributed to Ni^{2+} whereas the peaks at ~872.2 eV corresponds to the Ni^{2+} in Ni2$p_{1/2}$ region. In addition, two satellite peaks were also observed at ~861 eVand ~879.5 eV that are characteristics for materials containing Ni^{2+} species.[19-21] The core level Ni2*p* spectrum for $MnNi_2O_4$ showed a broad peak at 856.0 eV for Ni2$p_{3/2}$ and 873.8 eV for Ni2$p_{1/2}$ that is characteristics of Ni^{2+} and Ni^{3+} states with two satellite peaks at around 862.1 and 880.3 eV. The binding energy values reported here match very closely with the recently reported materials containing $Ni^{2+/3+}$ species.[22,23] The atomic ratio of Ni was also confirmed based on the areas of their corresponding XPS peaks.

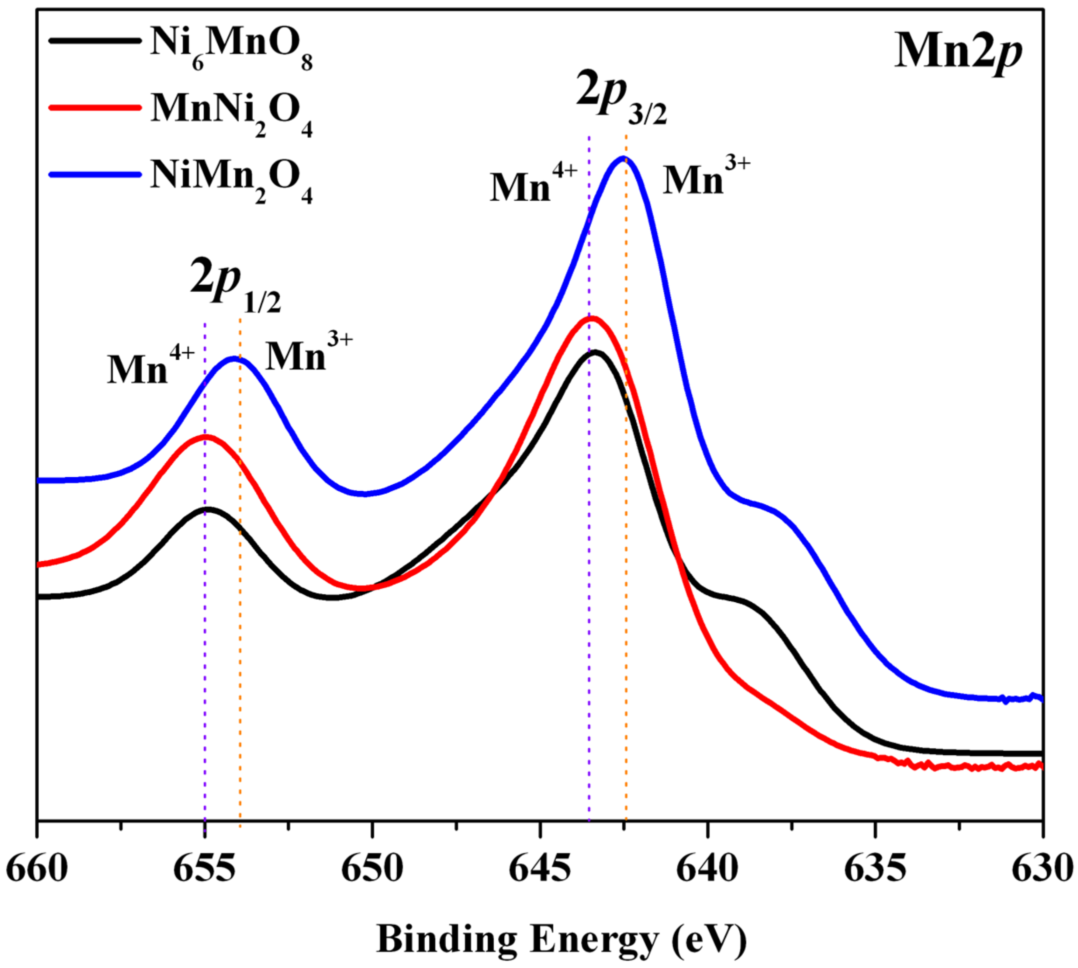

Figure S17. The XPS spectra of the regions containing the Mn2*p* of Ni_6MnO_8 and $MnNi_2O_4$, $NiMn_2O_4$. The Mn2*p* core level spectra of Ni_6MnO_8 and $MnNi_2O_4$ showed two major peaks with binding energies of ~643.5 eV and ~655.0 eV, and could be assigned to the Mn2$p_{3/2}$ and Mn2$p_{1/2}$ peaks, respectively.[24-27] The values obtained here are consistent with binding energies observed for MnO_2 confirming the presence of Mn^{4+} species. Similarly, the Mn 2*p* core level spectrum of $NiMn_2O_4$ displayes that Mn 2$p_{3/2}$ and Mn 2$p_{1/2}$ have binding energies centered at 642.4 eV and 653.9 eV, respectively. The results presented here agrees well with the literature reported materials containing Mn^{3+}.[23,24,28]

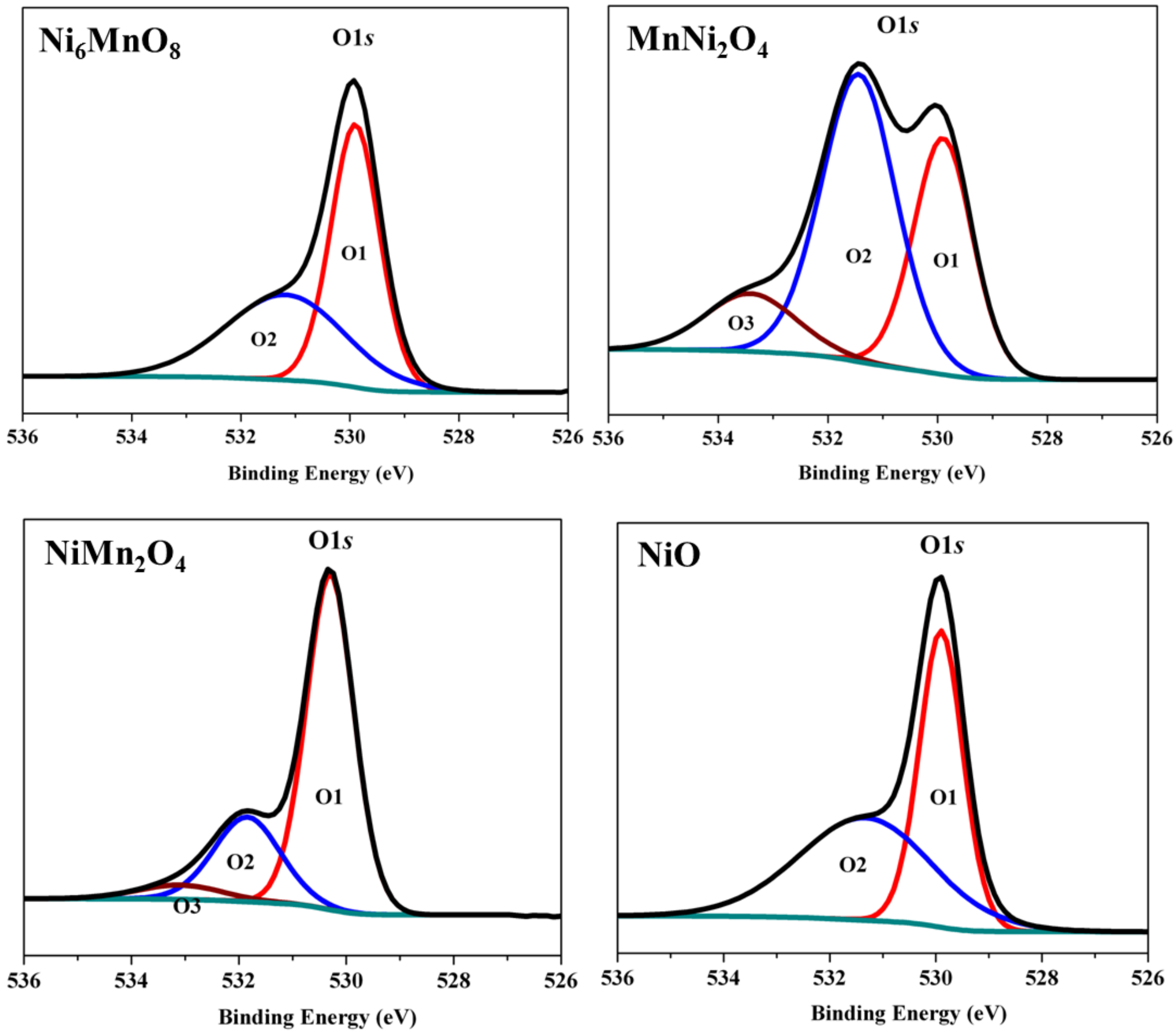

Figure S18. The XPS spectra of the regions containing the O1*s* of Ni_6MnO_8, $MnNi_2O_4$, $NiMn_2O_4$ and NiO. The O1*s* spectra of Ni_6MnO_8 and NiO were deconvoluted into two peaks. The peak at ~529.9 eV (O1) could be assigned to the oxygen atoms bound to oxides whereas a broad peak at ~531.5 eV (O2) is due to large dominance of –OH species absorbed on the surface either surface hydroxides or by the substitution of oxygen atoms at the surface by hydroxyl groups. In the case of $MnNi_2O_4$, and $NiMn_2O_4$, the peak at ~529.9 eV(O1) can be correlated to the metal oxygen bonds in while the peak at ~531.4 eV (O2) is attributed to the large amount of –OH species absorbed on the surface or C=O groups (for $MnNi_2O_4$) probably from the residues of oxalate precursor. The peak at ~533.2 eV (O3) is for the chemisorbed oxygen or adsorbed water molecules at the surface.[29-33]

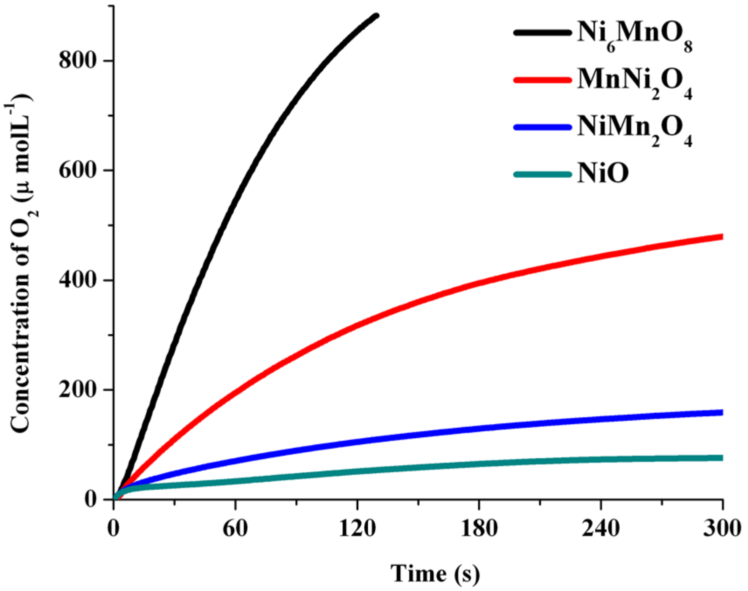

Figure S19. Dissolved oxygen concentrations were measured by a Clark electrode containing nickel manganese and nickel oxides catalysts and 0.5 M ceric ammonium nitrate (CAN) as an oxidant (catalyst amount is 1 mg).

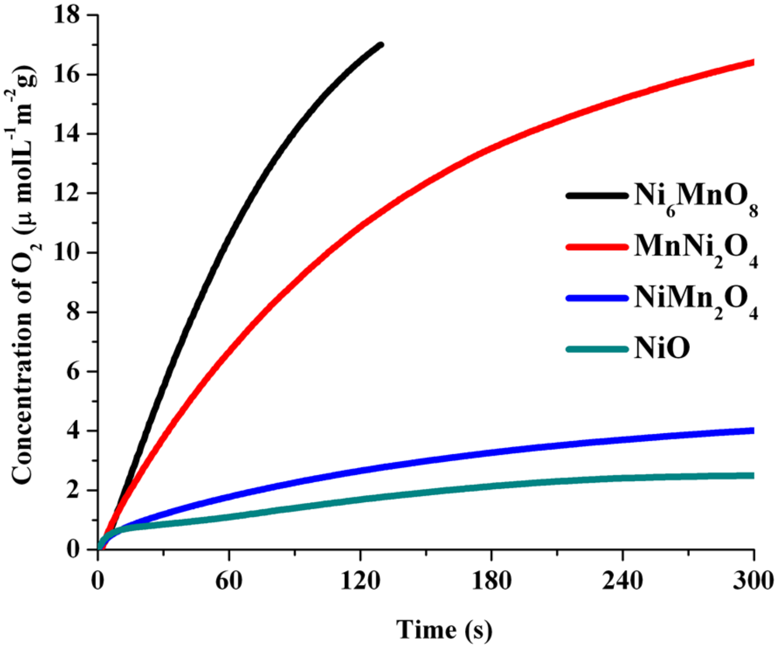

Figure S20. The surface-area normalised plot of oxidant-driven water oxidation with as synthesised nickel manganese oxides and nickel oxide which followed the same trend as that of Fig. S19.

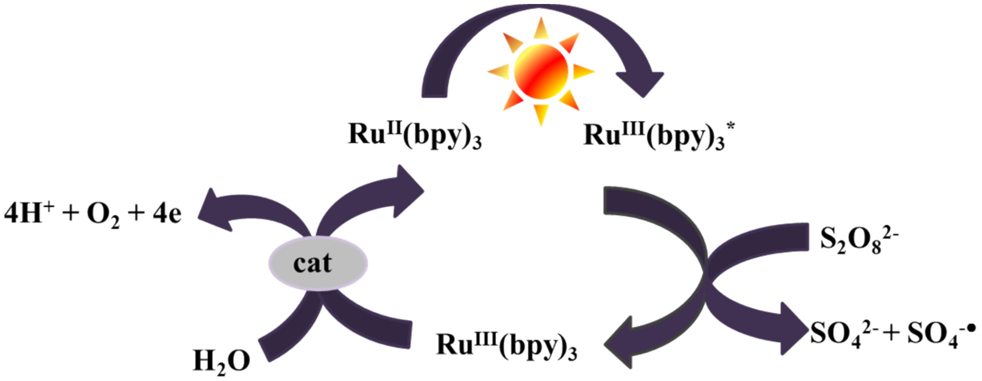

Scheme S1. Photocatalytic cycle of water oxidation with $Na_2S_2O_8$ and $[Ru(bpy)_3]^{2+}$ system. In the $Ru(bpy)_3]^{2+}$-$S_2O_8^{2-}$ system, the $[Ru(bpy)_3]^{2+}$ absorbs visible light and generates electron-hole pairs on the surface of the catalyst. The electrons produced were expelled by the sacrificial electron acceptor $S_2O_8^{2-}$ by further oxidising the $[Ru(bpy)_3]^{2+}$ to $[Ru(bpy)_3]^{3+}$ and reducing $S_2O_8^{2-}$ to SO_4^{2-} and a sulphate radical ($SO_4^{-\cdot}$). Thus the formed radical can subsequently further oxidise $[Ru(bpy)_3]^{2+}$ to yield $[Ru(bpy)_3]^{3+}$. Hence the $[Ru(bpy)_3]^{3+}$ molecule donates its holes to the catalyst and reverts back to the $[Ru(bpy)_3]^{2+}$ where two water molecules are oxidised to form one oxygen molecule. The dissolved O_2 content was analysed by a Clark oxygen electrode system.[34]

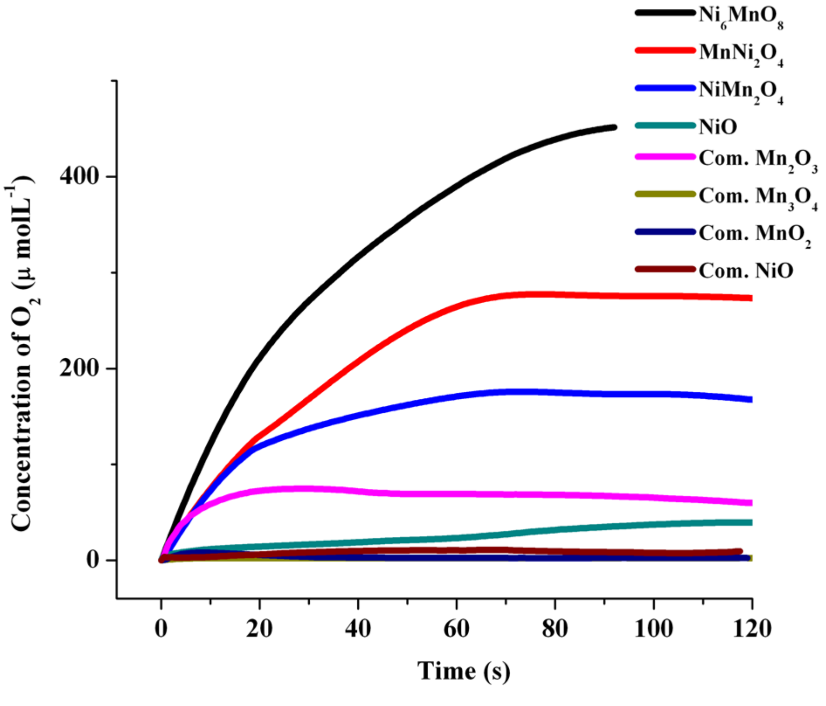

Figure S21. Dissolved oxygen concentrations of as synthesised nickel manganese oxides and nickel oxide catalysts against the commercial manganese and nickel oxides that were measured by a Clark electrode in phosphate buffer (pH = 7) using $Na_2S_2O_8$ as a two electron acceptor and $Ru(bpy)_3^{2+}$ as a photosensitiser (catalyst amount 0.5 mg).

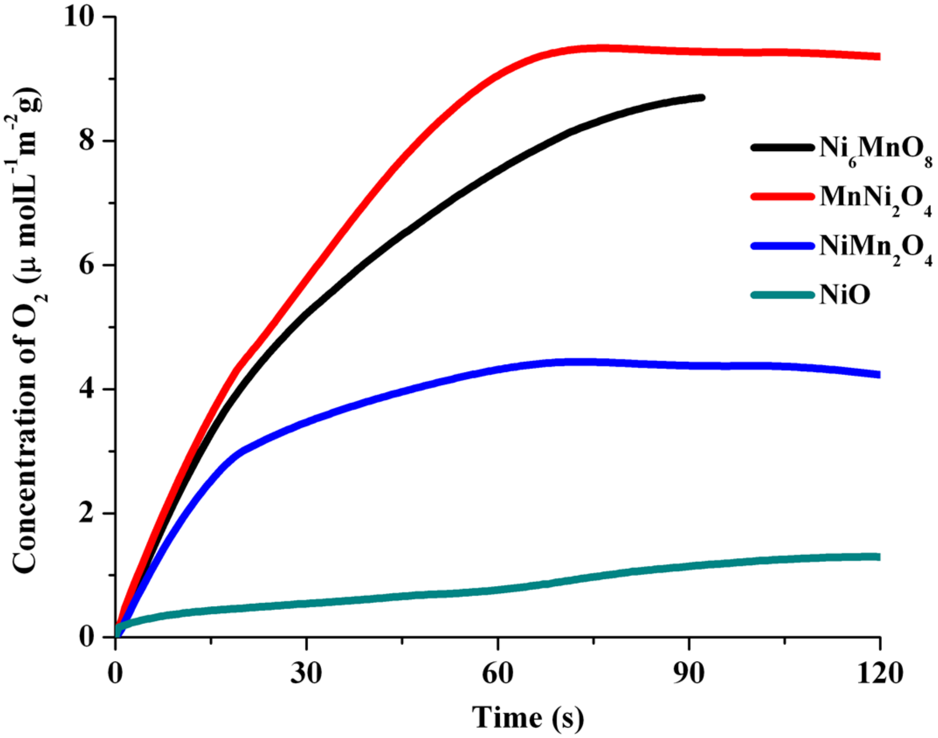

Figure S22. The surface-area normalised plot of oxidant-driven water oxidation with as synthesised nickel manganese oxides and nickel oxide. The $MnNi_2O_4$ showed higher activity due to its lower sufrace area.

Table S4. Summary of the oxidant-driven and photochemical activities of nickel manganese oxide catalysts.

Catalyst	S_{BET}[a]	O_2 evolution rate ($mmol_{O2}mol_M^{-1}s^{-1}$)[b]	
		Oxidant-driven	Photochemical
Ni_6MnO_8	51.9	1.41	1.00
$MnNi_2O_4$	29.2	0.52	0.69
$NiMn_2O_4$	39.6	0.19	0.44
NiO	30.4	0.15	0.07

[a] surface area in m^2/g, [b] the oxygen evolution rate was determined for the first 60 s

Table S5. Values of GC detection of oxygen gas in the head space of the reactor containing Ni_6MnO_8 and $MnNi_2O_4$ (see *SI*, Experimental section for details). The gas was collected after the photochemical experiments irradiated by xenon lamp for two hours. No hydrogen was detected.

Catalyst	Vol. % O_2 (with air)	Area O_2	Area N_2	Vol% O_2	Gas volume (mL)	O_2 (mL/h)	O_2 (µmol/h)
Ni_6MnO_8	1.49	95.52	91.13	0.711	14.25	0.075	3.12
	1.45	92.64	68.25	0.777	14.25	0.080	3.33
averaged	**1.47**	**94.08**	**79.69**	**0.744**	**14.25**	**0.078**	**3.23**
$MnNi_2O_4$	1.37	87.01	105.30	0.633	14.25	0.062	2.58
	1.33	84.09	72.86	0.737	14.25	0.070	2.91
	1.36	86.10	74.27	0.739	14.25	0.072	2.99
averaged	**1.35**	**85.73**	**84.14**	**0.703**	**14.25**	**0.068**	**2.83**

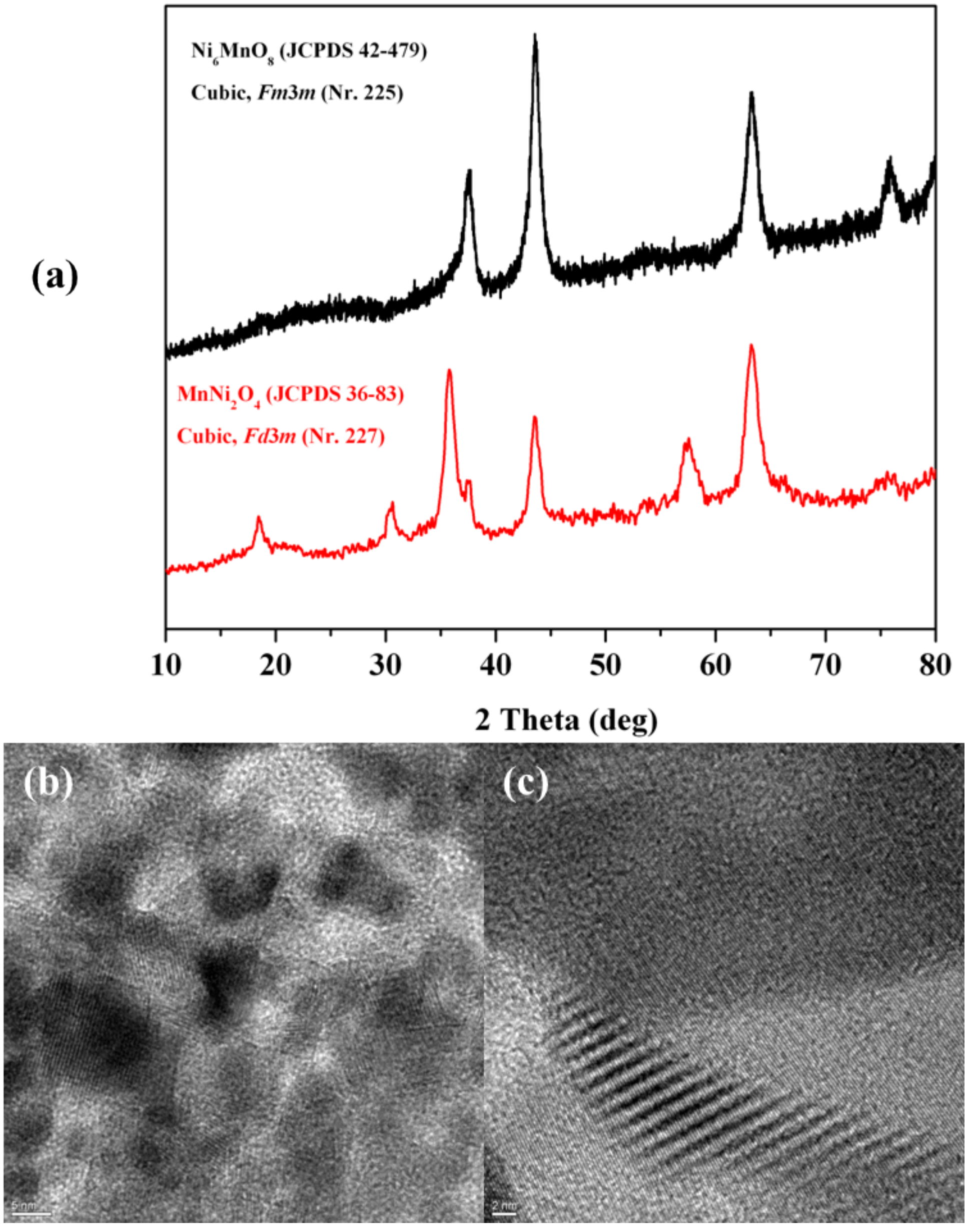

Figure S23. PXRD patterns (a), HRTEM images of the Ni_6MnO_8 (b) and $MnNi_2O_4$ (c) catalysts after the photocatalytic experiments in $Ru(bpy)_3]^{2+}$-$S_2O_8^{2-}$ system. Both XRD and TEM suggested that the crystallinity and the morphology of catalysts was retained after photo-catalysis indicationg higher stability.

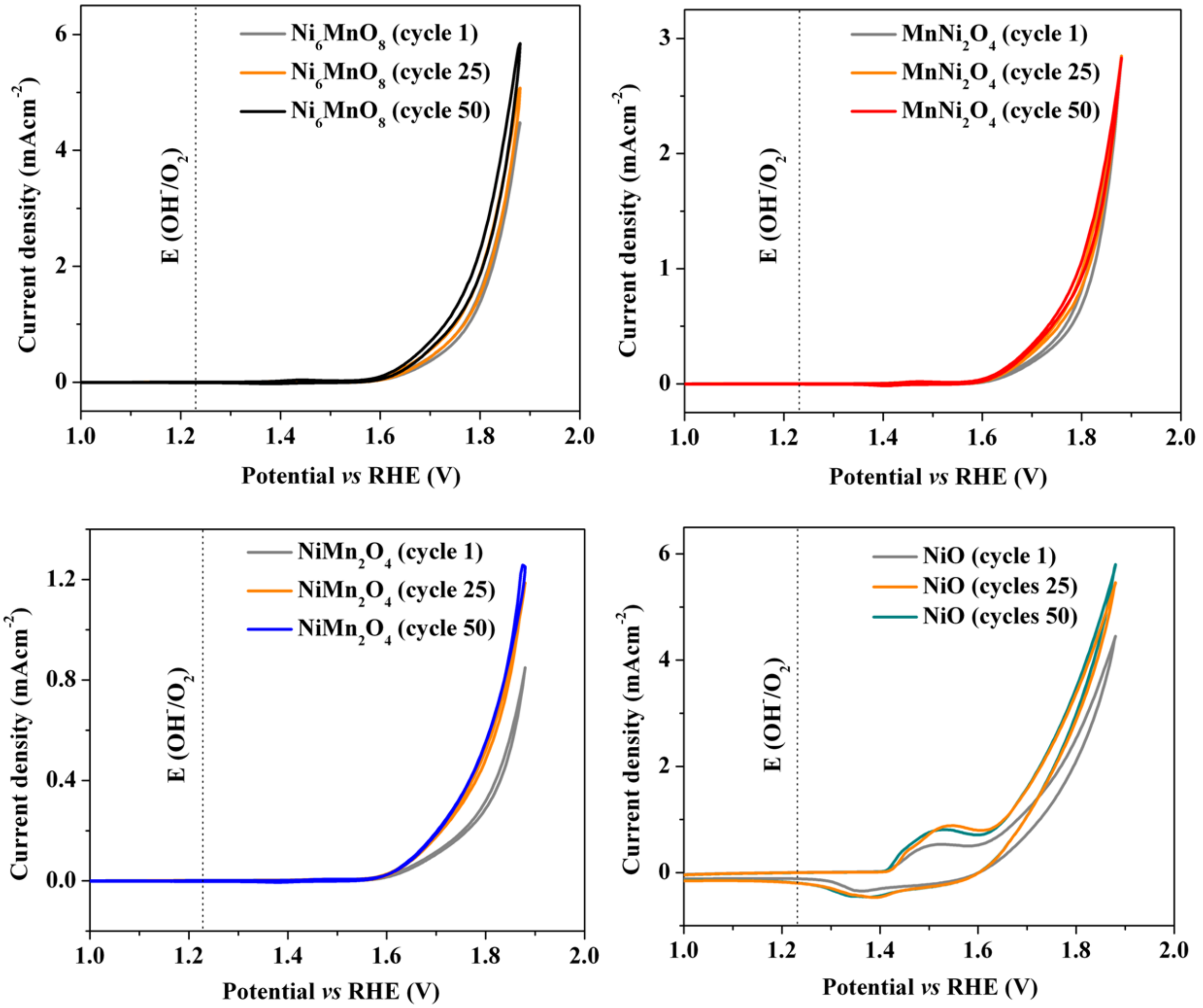

Figure S24. Cyclic voltammograms (sweep rate 20 mV/s) of Ni_6MnO_8, and $MnNi_2O_4$, $NiMn_2O_4$ and NiO thin films in 0.1 M KOH (pH 13) after 1st, 25th and 50th cycle. After 50th cycle the current density values became stable confirming that there is no additional phase transformation at the sufrace of the thin films.

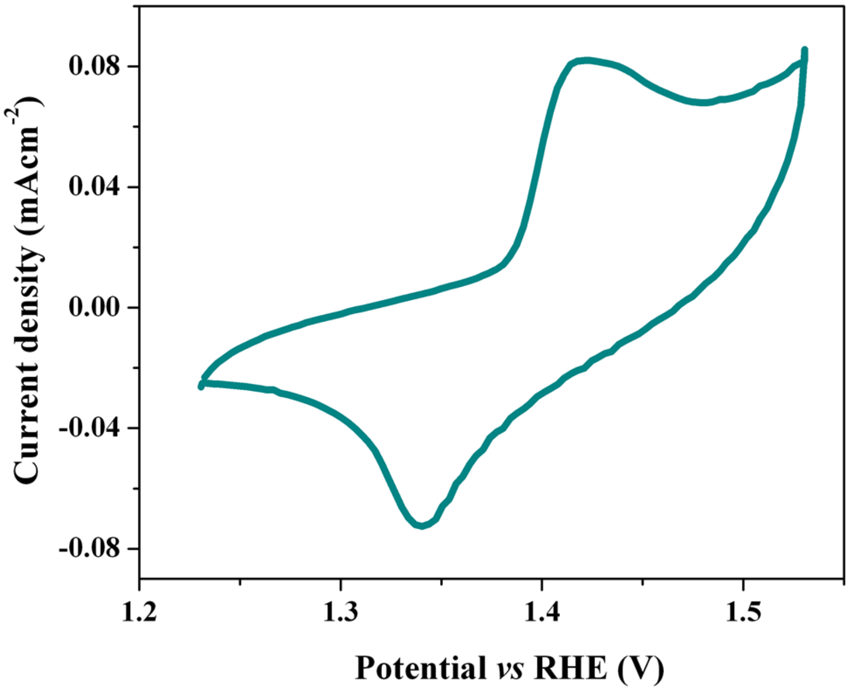

Figure S25. Cyclic voltammograms (sweep rate 20 mV/s) of NiO measured between 1.22 to 1.58 V (*Vs* RHE) in 0.1 M KOH at pH 13 featuring a pair of anodic and cathodic peaks corresponding to NiO/NiOOH.[35-38]

Table S6. Summary of the OER catalytic activities of nickel manganese and nickel oxide catalysts in 0.1 M KOH solution (pH 13).

Catalyst	$S_{BET}{}^{a}$	Overpotential at 1 mAcm^{-2}
Ni_6MnO_8	51.9	480
$MnNi_2O_4$	29.2	560
$NiMn_2O_4$	39.6	610
NiO	30.4	395

[a] surface area in m^2/g

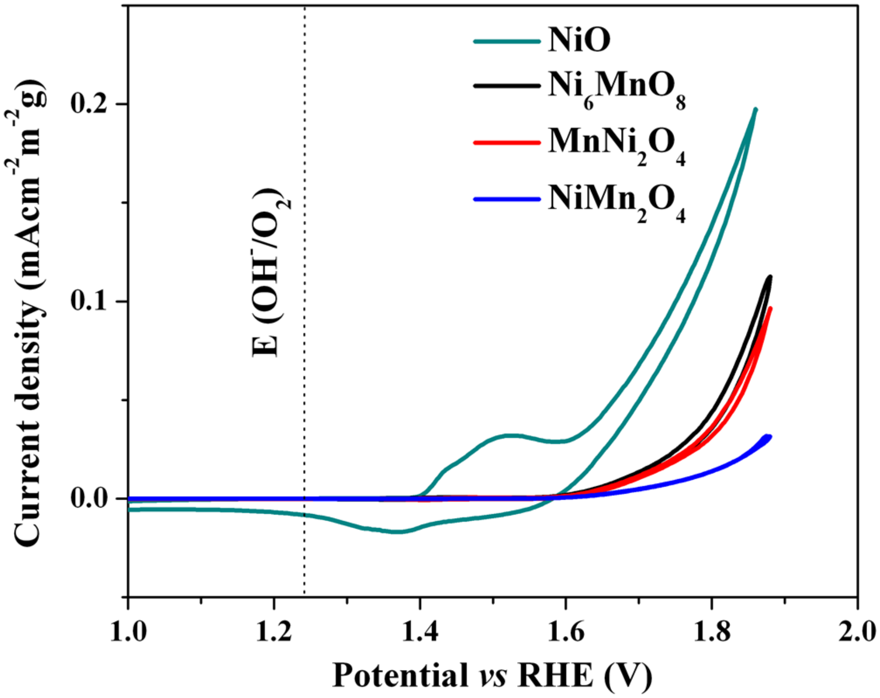

Figure S26. Cyclic voltammograms (sweep rate 20 mV/s) of Ni_6MnO_8, and $MnNi_2O_4$, $NiMn_2O_4$ and NiO thin films nornalised to sufrace area in 0.1 M KOH (pH 13)

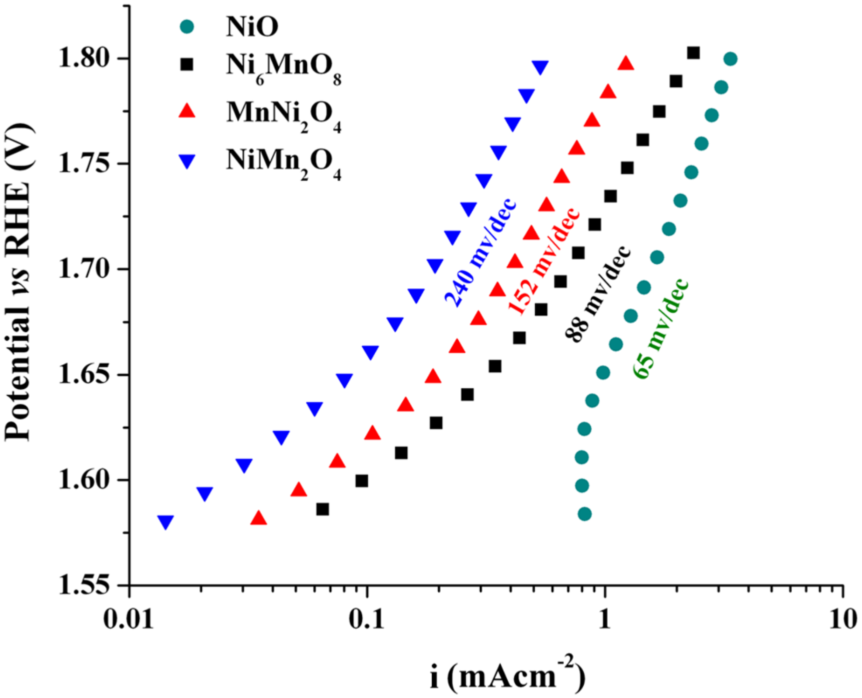

Figure S27. Tafel plot of the nickel manganese based catalysts in 0.1 M KOH at pH 13.

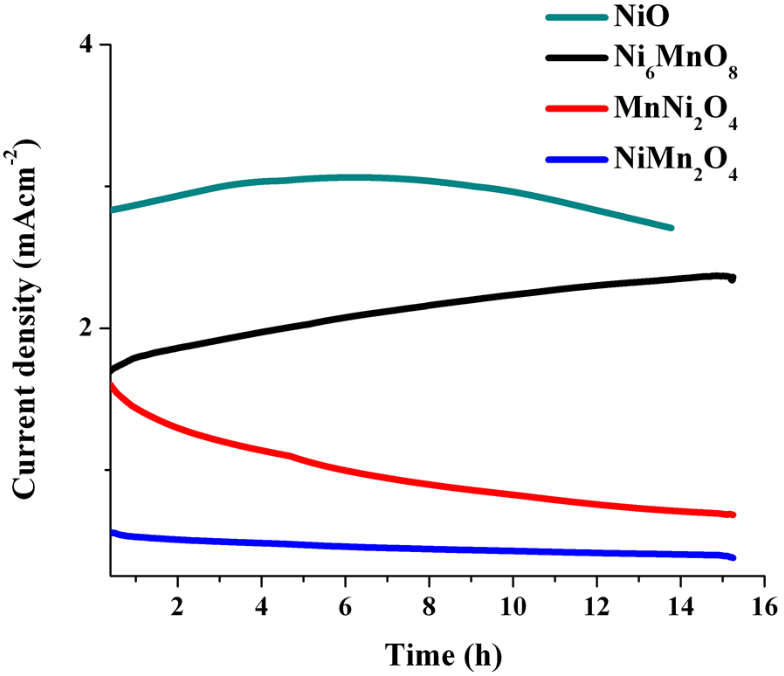

Figure S28. Current-time chronoamperometric responses of nickel manganese and nickel oxides measured at 1.8 V vs RHE in 0.1 M KOH solution.

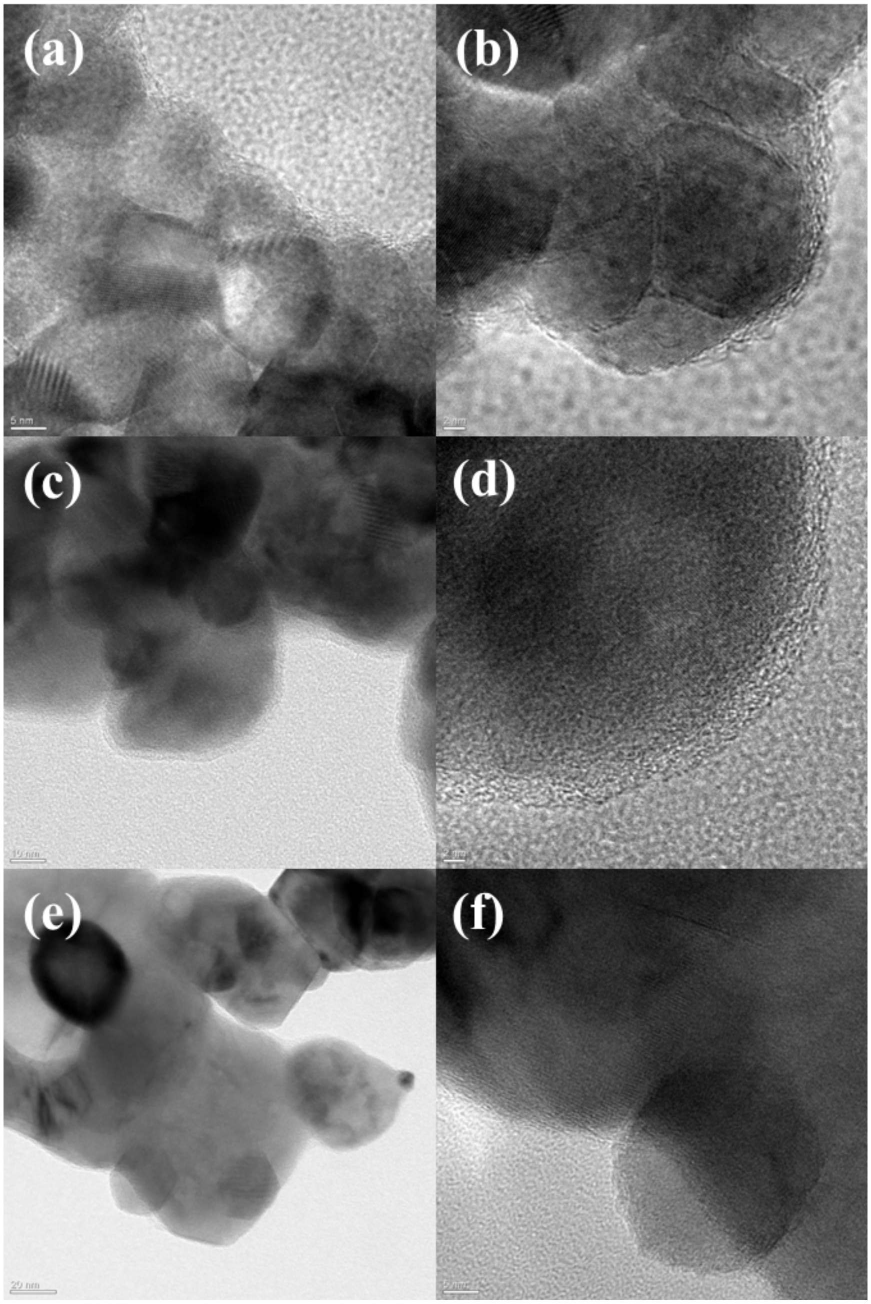

Figure S29. TEM and HRTEM images of the surface of the thin films of (a,b) NiO, (c,d) Ni_6MnO_8 and (e,f) $MnNi_2O_4$ after the chronoamperometric measurements in 0.1 M KOH solution. The higher resolution TEM images clearly show that a thin amorphous shell on the surface of the nanoparticles indicating formation of NiOOH phases as observed for other literature reported nickel based catalysts.[35,37]

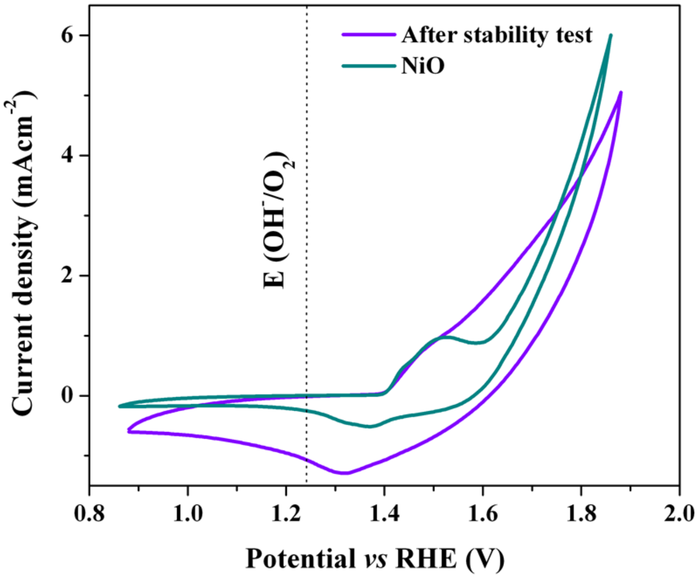

Figure S30. Cyclic voltammograms (sweep rate 20 mV/s) of NiO before and after the stability tests in 0.1 M KOH solution. The lower current density of NiO after stability test is presumably due to the deactivation of the catalyst after the long run.

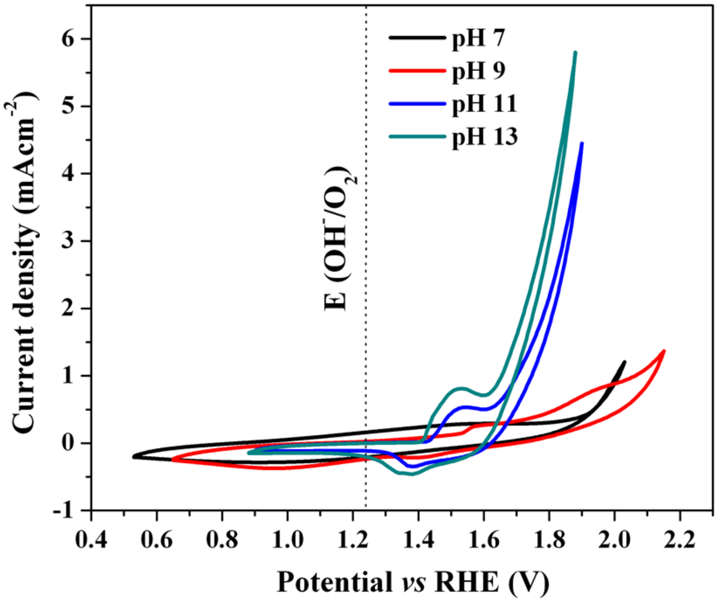

Figure S31. Cyclic voltammograms (sweep rate 20 mV/s) of NiO in phosphate (pH 7), borate (pH 9) buffers and in KOH (pH 11 and 13) solution. In all cases, the redox peaks corresponding to NiOOH were observed but resulting in lower activity at lower pH.

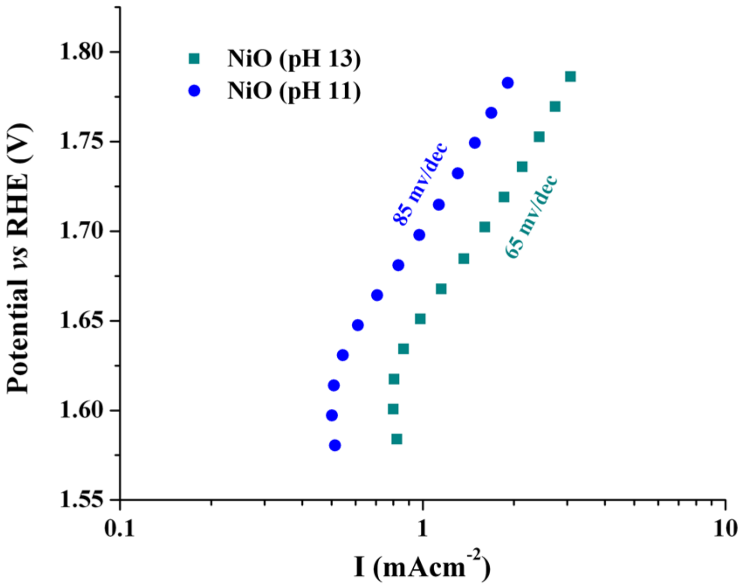

Figure S32. Tafel plots of the nickel oxide conducted in KOH solution at pH 13and pH 11. At lower pH, slower kinetics was observed.

.

Table S7. Comparison of OER data of Ni containing oxides.

Catalyst	electrolyte	Overpotential (mV)	Reference
Ni_6MnO_8	**0.1 M KOH**	**480[a]**	**This work**
$MnNi_2O_4$	**0.1 M KOH**	**560[a]**	**This work**
$NiMn_2O_4$	**0.1 M KOH**	**610[a]**	**This work**
NiO	**0.1 M KOH**	**395[a]**	**This work**
NiO_x electrodeposited	Phosphate buffer	650[a]	39
NiO_x electrodeposited	Borate buffer	630[a]	39
NiO_x	0.5 M KOH	305[a]	40
NiO_x	1 M KOH	420[b]	41
$NiCeO_x$	1 M KOH	280[b]	41,42
$NiCoO_x$	5 M KOH	400[b]	43
$NiCoO_x$	1 M NaOH	325[b]	44
$NiCuO_x$	1 M NaOH	420[b]	45
$NiFeO_x$	1 M KOH	290[b]	46
$NiLaO_x$	1 M KOH	360[b]	41

[a] 1 mA/cm^{-2}, [b] 10 mA/cm^{-2}

References

1. P. W. Menezes, A. Indra, P. Littlewood, M. Schwarze, C. Gobel, R. Schomacker and M. Driess, *ChemSusChem*, 2014 **7**, 2202-2211.
2. A. Indra, P. W. Menezes, I. Zaharieva, E. Baktash, J. Pfrommer, M. Schwarze, H. Dau and M. Driess, *Angew. Chem. Int. Ed.*, 2013, **52**, 13206-13210.
3. F. Jiao and H. Frei, *Angew. Chem. Int. Ed.*, 2009, **48**, 1841-1844.
4. F. Jiao and H. Frei, *Energy Environ. Sci.*, 2010, **3**, 1018-1027.
5. F. Jiao and H. Frei, *Chem. Commun.*, 2010, **46**, 2920-2922.
6. R. Deyrieux, C. Berro and A. Peneloux, *Bull. Soc. Chim. Fr.* , 1973, 25-34.
7. M. Latorre-sacnchez, P. Atienzar, G. Abellan, M. Puche, V. Fornes, A. Ribera and H. Garciaq, *Carbon*, 2012, **50**, 518-525.
8. B. Malecka, A. Malecki, E. Drozdz-Ciesla, L. Tortet, P. Llewellyn and F. Rouquerol, *Thermochimi. Acta*, 2007, **466**, 57-62.
9. Menaka, N. Garg, S. Kumar, D. Kumar, K. V. Ramanujachary, S. E. Lofland and A. K. Ganduly, *J. Mater. Chem.* , 2012, **22**, 18447-18453.
10. D. Wang, Q. Wang and T. Wang, *Inorg. Chem.*, 2011, **50**, 6482-6492.
11. M. Salavati-Niasari, N. Mir and F. Davar, *J. Phys. Chem. Solids*, 2009, **70**, 847-852.
12. S. A. A. Mansour, *Thermochim. Acta*, 1993, **230**, 243-257.
13. B. R. Shen, H. Shen, Y. X. Pan, T. F. Chen and X. E. Cai, *Z. Phys. Chem.*, 2001, **215**, 1413-1418.
14. W. Xiong, S. Jimei, G. Lisheng, J. Jiayi, Z. Huagui and Z. Zude, *Nanotechnology*, 2005, **16**, 37-39.
15. S. Sasaki, K. Fujino and Y. Takeuchi, *Proc. Jpn. Acad., Ser. B*, 1979, **55**, 43-48.
16. S. Asbrink, A. Waskowska, M. Drozd and E. Talik, *J. Phys. Chem. Solids*, 1997, **58**, 725-729.
17. P. Porta, G. Minelli, I. L. Botto and E. J. Baran, *J. Solid State Chem.*, 1991, **92**, 202-207.
18. A. B. Devale and D. K. Kulkarni, *J. Phys. C*, 1982, **15**, 899-905.
19. Y. S. Chen, J. F. Kang, B. Chen, B. Gao, L. F. Liu, X. Y. Liu, Y. Y. Wang, L. Wu, H. Y. Yu, J. Y. Wang, Q. Chen and E. G. Wang, *J. Phys. D*, 2012, **45**, 065303.
20. D.-H. Shin, J.-S. Lee, J. Jun and J. Jang, *J. Mater. Chem. A.* , 2014, **2**, 3364-3371.
21. R. S. C. Smart, A. P. Grosvenor, M. C. Biesinger and N. S. McIntyre, *Surf. Sci.*, 2006, **600**, 1771-1779.
22. B. Yan, J. Liu, B. Song, P. Xiao and L. Lu, *Sci. Rep.*, 2013, **3**.
23. W. Kang, Y. Tang, W. Li, X. Yang, H. Xue, Q. Yang and C.-S. Lee, *Nanoscale*, 2014, DOI: 10.1039/C4NR04031.
24. L. Hernan, J. Morales, L. Sanchez, E. R. Castellon and M. A. G. Aranda, *J. Mater. Chem.*, 2002, **12**, 734-741.

25. S. W. Lee, J. Kim, S. Chen, P. T. Hammond and Y. Shao-Horn, *ACS Nano*, 2010, **4**, 3889-3896.
26. M. C. Biesinger, B. P. Payne, A. P. Grosvenor, L. W. M. Lau, A. R. Gerson and R. S. C. Smart, *Appl. Surf. Sci.*, 2011, **257**, 2717-2730.
27. M. C. Biesinger, B. P. Payne, B. R. Hart, A. P. Grosvenor, N. S. McIntryre, L. W. M. Lau and R. S. C. Smart, *Surf. Interface Anal.* , 2009, **41**, 324-332.
28. H. W. Nesbitt and D. Banerjee, *Am. Mineral.*, 1998, **83**, 305-315.
29. V. M. Jimenez, A. Fernandez, J. P. Espinos and A. R. Gonzalezelipe, *J. Electron Spectrosc. Relat. Phenom.*, 1995, **71**, 61-71.
30. M. Elbaydi, S. K. Tiwari, R. N. Singh, J. L. Rehspringer, P. Chartier, J. F. Koenig and G. Poillerat, *J. Solid State Chem.*, 1995, **116**, 157-169.
31. J. F. Marco, J. R. Gancedo, M. Gracia, J. L. Gautier, E. Rios and F. J. Berry, *J. Solid State Chem.*, 2000, **153**, 74-81.
32. X. Yuan, M. Zhang, X. Chen, N. An, G. Liu, Y. Liu, W. Zhang, W. Yan and M. Jia, *Appl.Catal. A*, 2012, **439**, 149-155.
33. V. Shinde, A. B. Mandale, K. R. Patil, A. B. Gaikwad and P. P. Patil, *Surf. Coat. Technology*, 2006, **200**, 5094-5101.
34. A. Harriman, I. J. Pickering, J. M. Thomas and P. A. Christensen, *J. Chem. Soc. Farad. Trans.*, 1988, **84**, 2795-2806.
35. M. Gao, W. Sheng, Z. Zhuang, Q. Fang, S. Gu, J. Jiang and Y. Yan, *J. Am. Chem. Soc.*, 2014, **136**, 7077-7084.
36. I. M. Sadiek, A. M. Mohammad, M. E. El-Shakre and M. S. El-Deab, *Int. J. Hydrogen Energy*, 2012, **37**, 68-77.
37. K. Fominykh, J. M. Feckl, J. Sicklinger, M. Doeblinger, S. Boecklein, J. Ziegler, L. Peter, J. Rathousky, E.-W. Scheidt, T. Bein and D. Fattakhova-Rohlfing, *Adv. Funct. Mater.*, 2014, **24**, 3123-3129.
38. M. E. G. Lyons and M. P. Brandon, *Int. J. Electrochem. Sci.*, 2008, **3**, 1386-1424.
39. M. Risch, K. Klingan, J. Heidkamp, D. Ehrenberg, P. Chernev,I. Zaharieva and Holger Dau, *Chem. Commun.*, 2011, **47**, 11912–11914.
40. K. Fominykh, J. M. Feckl, J. Sicklinger, M. Doeblinger, S. Boecklein, J. Ziegler, L. Peter, J. Rathousky, E.-W. Scheidt, T. Bein and D. Fattakhova-Rohlfing, *Adv. Funct. Mater.*, 2014, **24**, 3123-3129.
41. D. A. Corrigan and R. M.Bendert, *J. Electrochem. Soc.* 1989, **136**, 723−728.
42. C. C. L. McCrory, S. Jung J. C. Peters, and Thomas F. Jaramillo, *J. Am. Chem. Soc.* 2013, **135**, 16977−16987
43 J. C. K Ho and D. L. Piron, *J. Appl. Electrochem*. 1996, 26, 515−521.
44 Y. Yang, H. Fei, G. Ruan, C. Xiang and J. M. Tour, *ACS Nano*, 2014, **8**, 9518–9523
45 X. Li, F. C. Walsh and D. Pletcher, *Phys. Chem. Chem. Phys.* 2011, **13**, 1162−1167
46 M. D. Merrill and R. C. Dougherty, *J. Phys. Chem. C* 2008, **112**, 3655−3666.